SIMPLEX CODED RAMAN OTDR-BASED DISTRIBUTED TEMPERATURE SENSING

A THESIS SUBMITTED TO

THE GRADUATE SCHOOL OF ENGINEERING AND SCIENCE

OF BILKENT UNIVERSITY

IN PARTIAL FULFILLMENT OF THE REQUIREMENTS FOR

THE DEGREE OF

MASTER OF SCIENCE

IN

MATERIALS SCIENCE AND NANOTECHNOLOGY

By

Buğra Yalçın

June 2025

Simplex Coded Raman OTDR-Based Distributed Temperature Sensing
By Buğra Yalçın
June 2025

We certify that we have read this thesis and that in our opinion it is fully adequate, in scope and in quality, as a thesis for the degree of Master of Science.

Ekmel Özbay(Advisor)

İbrahim Tuna Özdür

Hasan Yılmaz

Approved for the Graduate School of Engineering and Science:

Orhan Arıkan
Director of the Graduate School

ABSTRACT

SIMPLEX CODED RAMAN OTDR-BASED DISTRIBUTED TEMPERATURE SENSING

Buğra Yalçın
M.S. in Materials Science and Nanotechnology
Advisor: Ekmel Özbay
June 2025

Temperature sensing for environmental and structural monitoring is of utmost importance for certain applications, e.g., monitoring of wildfires, gas pipelines, electric lines, temperature of facilities such as nuclear reactors, etc. Conventional devices to measure temperature along many kilometers are not cost-effective, and are impractical to install each measurement device. The solution heralded was to utilize the back-scattered Raman signal inside the optical fiber to measure the temperature, as the Raman scattering is a manifestation of the interaction of light with molecular vibrations (optical phonons). Each scattering point along the fiber serves as an individual sensing element, and for that reason, this technology is called 'Distributed Temperature Sensing' (DTS).

However, the problem with Raman OTDR-based DTS originates due to the Raman signal being weak as much as $70dB$ below the launched optical power, resulting in a low signal-to-noise ratio (SNR). Increasing optical power is not viable because of optical nonlinearities. To overcome this problem, advanced noise filtering techniques and interrogation methods can be used. An interrogation method named Simplex coding is widely used in the literature, which involves the modulation of the amplitude of the laser, based on a predetermined code word. In this way, more than one pulse can be present during each interrogation, which then suppresses the uncorrelated additive white Gaussian noise. Optimizing the SNR enables longer sensing distances and higher temperature resolution performance in Raman OTDR-based DTS systems.

In this thesis, first, a commonly used Wavelet-transformation-based denoising is experimentally demonstrated in a multi-mode fiber equipped RDTS system. The method has improved the temperature resolution from $0.45°C$ to $0.10°C$ at

$5.5km$. Finally, 7-bit Simplex coding is experimentally demonstrated in a single-mode fiber equipped RDTS system. The Simplex coding method has improved the temperature resolution from $1.3°C$ to $0.8°C$ at $5km$.

Keywords: Distributed temperature sensor, optical time domain reflectometer, Raman scattering, fiber optics..

ÖZET

SIMPLEX KODLANMIŞ RAMAN OTDR-TABANLI DAĞITIK SICAKLIK ALGILAMA

Buğra Yalçın
Malzeme Bilimi ve Nanoteknoloji, Yüksek Lisans
Tez Danışmanı: Ekmel Özbay
Haziran 2025

Çevresel ve yapısal izleme amacıyla sıcaklık algılaması, orman yangınları, gaz boru hatları, elektrik hatları ve nükleer reaktörler gibi tesislerin sıcaklık kontrolü gibi bazı uygulamalarda son derece önemlidir. Sıcaklık ölçümü yapabilen geleneksel cihazları uzun kilometreler boyunca kullanmak maliyet açısından verimli olmamakla beraber her bir ölçüm noktasına ayrı sensör yerleştirmek de pratik değildir. Bu soruna getirilen çözüm, optik fiber içindeki geri saçılan Raman sinyalinin kullanılmasıdır. Çünkü Raman saçılması, ışığın moleküler titreşimlerle (optik fononlarla) etkileşiminin bir sonucudur. Fiber boyunca bulunan her saçılma noktası, ayrı birer sensör görevi görür ve bu nedenle bu teknoloji "Dağıtık Sıcaklık Algılama (DTS)" olarak adlandırılır.

Ancak, Raman OTDR tabanlı DTS (RDTS) sistemlerindeki temel sorun, Raman sinyalinin fibere giren optik güce kıyasla yaklaşık $70dB$ daha zayıf olmasıdır; bu da düşük bir sinyal-gürültü oranına (SNR) neden olur. Optik gücü artırmak ise doğrusal olmayan optik etkiler nedeniyle mümkün değildir. Bu sorunun üstesinden gelmek için gelişmiş gürültü filtreleme teknikleri ve sorgulama yöntemleri kullanılabilir. Literatürde yaygın olarak kullanılan bir sorgulama yöntemi olan Simplex kodlama, lazerin genliğini önceden belirlenmiş bir kod dizinine göre modüle eder. Bu şekilde, her bir sorgulamada birden fazla optik darbe gönderilebilir ve bu da ilişkisiz toplanır beyaz Gauss gürültüsünü bastırır. SNR'ın optimize edilmesi, RDTS sistemlerinde daha uzun algılama mesafeleri ve daha yüksek sıcaklık çözünürlüğü sağlar.

Bu tezde, ilk olarak çok modlu fiber kullanılan bir RDTS sisteminde yaygın bir yöntem olan Wavelet dönüşümüne dayalı gürültü filtreleme yöntemi deneysel olarak gösterilmiştir. Bu yöntem, $5.5km$ ölçüm mesafesindeki sıcaklık

çözünürlüğünü 0.45°C'den 0.10°C'ye iyileştirmiştir. Son olarak, tek modlu fiber kullanılan bir RDTS sisteminde 7-bitlik Simplex kodlama deneysel olarak uygulanmıştır. Bu yöntemle ise 5km ölçüm mesafesindeki sıcaklık çözünürlüğü 1.3°C'den 0.8°C'ye iyileştirilmiştir.

Anahtar sözcükler: Dağıtık sıcaklık sensörü, optik zaman alanı reflektometresi, Raman saçılımı, fiber optik..

Acknowledgement

I would like to present my sincere gratitude and thanks to my thesis advisor, Prof. Ekmel Özbay for his support, guidance, and understanding throughout my research. I will always admire his hard work and the work environment he created at NANOTAM. His vision and passion for his work made a strong impression on me. I would also present my gratitude to Dr. Tolga Kartaloğlu for his continuous feedback and support throughout my research. Their guidance helped me to achieve an engineering-oriented perspective.

I would also like to thank Assoc. Prof. Hasan Yılmaz for accepting to be on my graduate committee. I am grateful to him for sharing his experience with me when I was struggling at the beginning of my master's. His positive influence on me has helped me to cope with struggles.

I would like to thank all my colleagues at NANOTAM, especially Volkan Türker, Faruk Uyar, Ömer Faruk Dinç, Gülşah Yıldız, Abdulhay Can Kara, Dora Pancar, Kaan Doğan, Reham Elshurafa and Serra Uluğ for their support and friendship.

However, I am grateful most to my family, my mother Arzu, grandmother Müzeyyen, and cousins Tuncay and Öykü for their unconditional love. Finally, I would like to thank my closest and dearest friends Arda, Baran, Umut, Özden, Mihriban, Tuna and Gizem, who have always been there for me.

Contents

List of Figures

List of Tables

Chapter 1

Introduction

Since the invention of optical fibers, they have become indispensable in today's technology, finding applications in communication networks, fiber-based lasers, sensors, navigation, biomedical imaging, holography, neural networks, and beyond [1–8]. Their unique properties, such as ultra-low loss, high-speed signal transmission, and broad bandwidth, make them ideal for diverse uses. While optical fibers primarily function as waveguides for transmitting light, the light propagating through them interacts with the medium in various ways - nonlinear optical effects, scattering, and dispersion, to name a few. Depending on the application, these interactions can be harnessed or mitigated to achieve specific objectives, e.g., while modulation instability is a desired nonlinear optical effect in supercontinuum generation [9], it is an unwanted effect in distributed fiber optical sensor (DFOS) technology.

Among these phenomena, the scattering of light plays a pivotal role in DFOS technology. Namely, Rayleigh, Brillouin, and Raman scattering are the foundation for DFOSs [10]. In the context of temperature sensing, Raman scattering - resulting from the interaction of light with molecular vibrations (optical phonons) - is the primary physical phenomenon. Because molecular vibrations are influenced by temperature, the intensity of Raman scattered light provides a reliable indicator of thermal conditions. Combining Raman scattering with the optical time-domain reflectometry (OTDR) principle allows for spatially resolved temperature sensing along the length of the fiber. Each scattering point within the fiber effectively serves as an individual sensing element, enabling a single fiber to host thousands of virtual sensors. And the nomenclature of ***distributed sensing*** is derived from this fact.

The demand for ***distributed temperature sensing (DTS)*** arises from the need to monitor extensive or inaccessible areas, such as nuclear reactors [11], tunnels [12], oil and gas pipelines [13], railways [14], and power distribution lines [15]. While effective in localized regions, conventional temperature sensors are impractical and cost-prohibitive for covering such large-scale environments. Raman OTDR-based DTS (RDTS) systems, with their ability to provide high temperature resolution and cost-effective and spatially distributed temperature monitoring, offer an intelligent solution to this problem. The figure below shows the difference between traditional sensing and distributed fiber optical sensing.

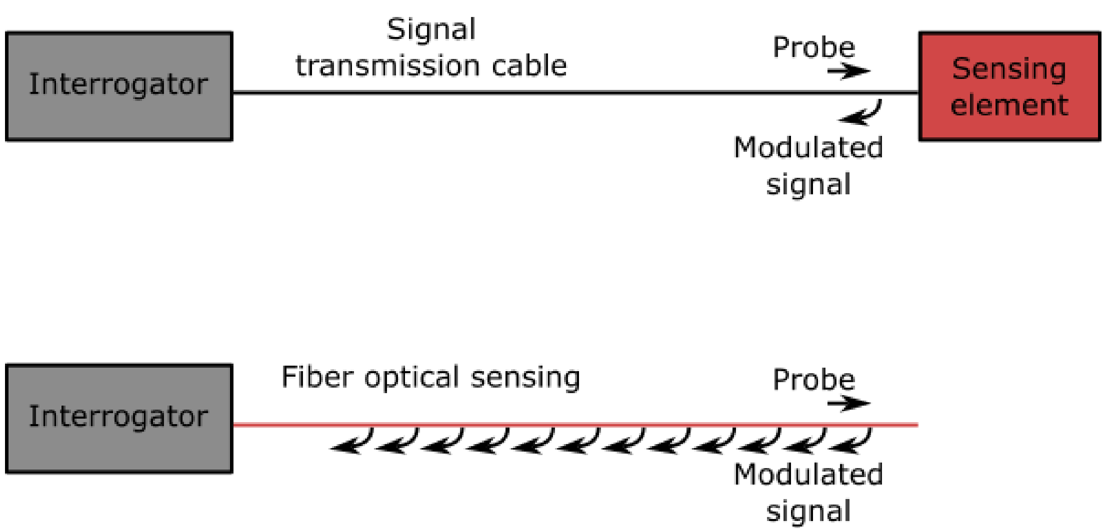

Figure 1.1: Difference between traditional sensing and distributed fiber optical sensing.

RDTS was first theoretically proposed by Dakin et al. [16] in 1985. Later that same year, they experimentally demonstrated the technology [17]. Figure 1.2 shows a typical experimental setup for the RDTS system. Over the years, the measurement performance of RDTS is mainly characterized by temperature accuracy, temperature resolution, spatial resolution, and sensing distance. These performance metrics are determined by pulse duration, peak power of the optical pulse, advanced measurement, and post-processing techniques such as denoising [18]. Among the scattering mechanisms, Raman scattering is the weakest in optical power, being as weak as $70dB$ below the launched optical power [19], making it challenging to obtain a high signal-to-noise ratio (SNR) at further distances. Increasing the optical power is not viable due to the onset of optical nonlinearities, e.g., *modulation instability, stimulated Raman scattering (SRS)*, etc. To overcome these challenges, advanced denoising methods and advanced interrogation methods such as double-ended sensing [20], pulse coding [21] are suggested in the literature. On the other hand, to increase the spatial resolution of RDTS systems, Li et al. suggested a slope-assisted measurement method [22] and a chaotic correlation demodulation method [23]. Among all the developments, the pulse coding method was widely used in industrial products to increase sensing distance [24]. This method modulates the laser amplitude with respect to a predetermined binary codeword. Instead of using a single pulse for interrogation, it uses a series of optical pulses based on the binary codeword. By doing so, it increases the SNR of the system under the same measurement duration to that of traditional interrogation —single pulse.

Different pulse coding methods have been suggested in the literature, including a novel coding scheme based on genetic algorithm proposed by Sun et al. [25]. The most common methods are Simplex coding [26] and Golay coding [27], which are based on linear coding and correlation-based coding, respectively. Correlation-based codes have been widely used in radar systems over the past decades [28], especially for their advantage of increased spatial resolution. However, Simplex codes are less demanding than Golay codes regarding computational load. The increase in SNR is similar between the two methods.

This thesis adopts Wavelet denoising and Simplex coding from the literature,

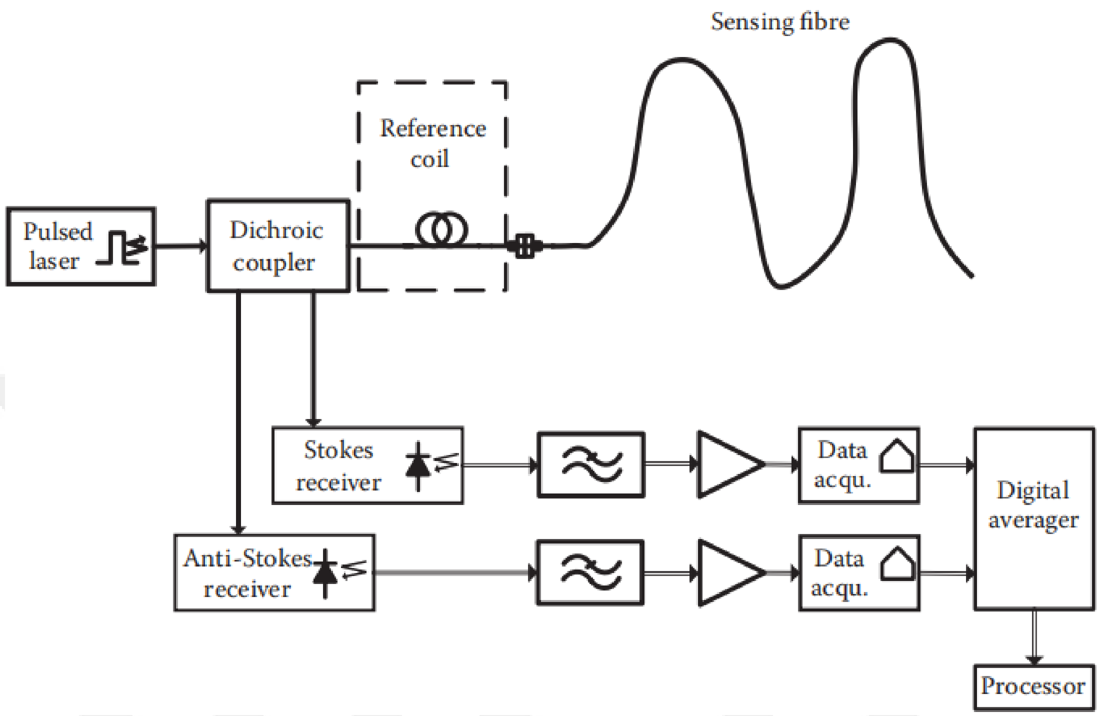

Figure 1.2: Schematics of a typical RDTS system (Adapted from [10]).

demonstrating their effectiveness in increasing the temperature measurement performance of RDTS systems. The next chapter provides the necessary theory before introducing how technology works. The latter section explains the RDTS technology in detail. Chapter 4 introduces the concept of pulse coding and explains the Simplex coding method in detail. The remaining part of the thesis presents experimental results, analysis, and system design.

Chapter 2

Theoretical Background

It is mentioned that optical fibers are superior due to their properties, such as ultra-low loss, high-speed signal transmission, and broad bandwidth. However, propagation of light inside an optical fiber should be well understood to study fiber-optic-based technologies. Various light-material interactions occur during propagation as a result of the optical properties of the fiber. Figure 2.1 shows the structure of a conventional optical fiber, where a core region is surrounded by cladding and protected by a coating. A very small difference between the refractive index of the core n_1 and the cladding n_2 causes light to be trapped inside the core along propagation. This phenomenon is known as total internal reflection (TIR) and is the physical origin of waveguiding.

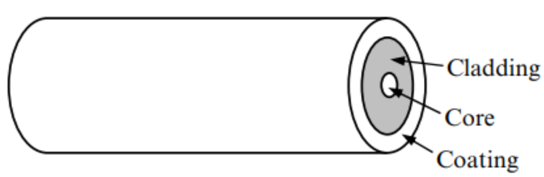

Figure 2.1: Conventional optical fiber.

It should be noted that this does not necessarily mean that the electromagnetic field propagates solely along the core; in fact, some extent of the electromagnetic field continues to propagate along the cladding. However, it is safe to say that most of the optical pulse is trapped inside the core region. The propagation of light can be discussed using geometrical optics to some extent. However, the wave equation is needed to understand how different modes of light propagate along the fiber.

Figure 2.2 shows the cross-sectional side view of a fiber where an incident beam of light enters the fiber with an angle of θ_1 with respect to the optical axis. The light gets refracted according to Snell's law whenever the refractive index changes. We should recall the condition for TIR, then,

$$n_0 sin\theta_1 = \sqrt{(n_1^2 - n_2^2)} \tag{2.1}$$

where equation (2.1) is the numerical aperture NA of the fiber, which determines the modal characteristics of the fiber, i.e., single-mode (SM) or multi-mode (MM) operation. A more general statement for determining whether the fiber is SM or MM is given by

$$V = \frac{2\pi a}{\lambda} NA \tag{2.2}$$

where a is the core radius, λ is the wavelength. Single-mode fibers (SMF) operate between $0 < V < 2.405$, while multi-mode fibers (MMF) operate at $V > 2.405$. As equation (2.2) suggests, SMFs have a smaller core radius than MMFs.

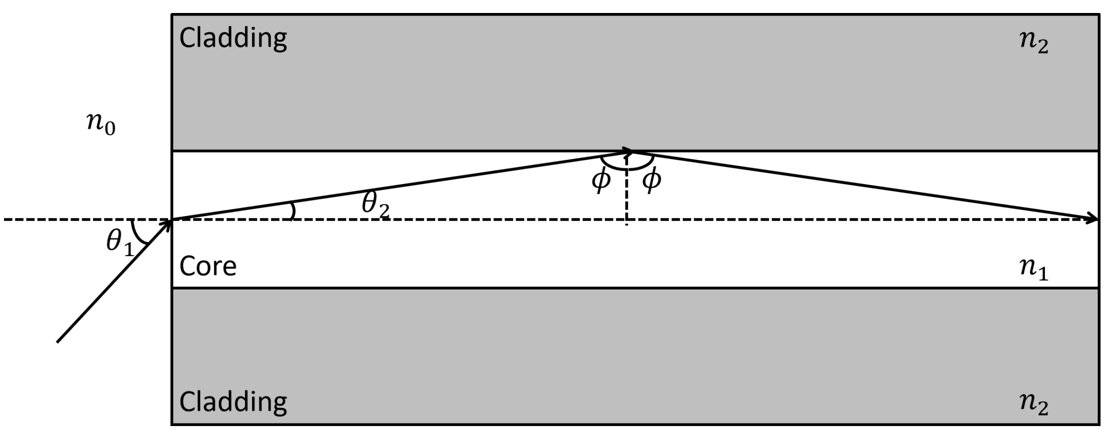

Figure 2.2: Cross-sectional side view of a fiber with a propagating beam inside.

The main material used in an optical fiber is silicon dioxide (SiO_2). However, there may be some dopants such as GeO_2, Al_2O_2 for certain applications. Thus, the dielectric function of the fiber is mainly determined by SiO_2, and it determines the refractive index, which is wavelength dependent. Due to this wavelength dependence, light gets dispersed over distance. As a result, an optical pulse becomes broader in the time domain as it continues to propagate. This phenomenon is known as group velocity dispersion (GVD). Because GVD is accumulative, it can be a limiting factor for certain applications, such as optical communications, as consecutive symbols will no longer be distinguished because of dispersion. To overcome this limitation, optical communications channels use dispersion compensation units. Apart from GVD, there are other types of dispersions as well, such as polarization mode dispersion (PMD) and modal dispersion. Whereas PMD is caused by imperfect cylindrical symmetry of the fiber, modal dispersion is due to the fact that each mode has different propagation velocities. Each of these effects can impose certain limitations on the performance of optical systems.

Another optical phenomenon occurring in the fiber is attenuation of light, mainly due to absorption and scattering. Attenuation is generally described by the Beer-Lambert law:

$$P(z) = P_0 e^{-\alpha z} \tag{2.3}$$

where $P(z)$, P_0, and α stand for optical power at distance z, initial optical power, and attenuation coefficient, respectively. Here, the contribution of absorption and scattering to total attenuation is tucked into α. Figure 2.3 shows the attenuation profile of a single-mode fiber with respect to wavelength.

Light scattering plays a pivotal role in DFOS technology. While acoustic and strain sensing utilize Rayleigh and Brillouin scattering, temperature sensing is mostly done with Raman scattering. There are DTS technologies that rely on Rayleigh and Brillouin scattering —LPR method. However, this thesis focuses on Raman scattering-based temperature sensing. Figure 2.4 illustrates the scattered light spectrum in a conventional SMF.

Each type of scattering originates through different mechanisms. However, they all depend on the fiber characteristics. Rayleigh scattering is the result

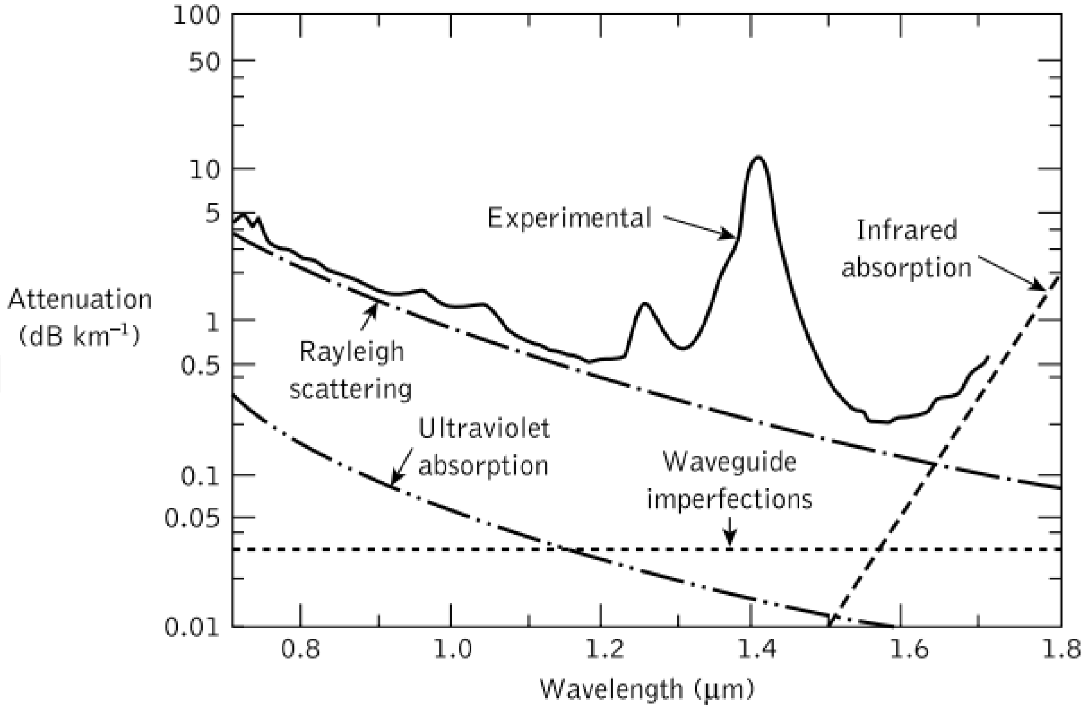

Figure 2.3: Attenuation profile of a conventional SMF (Adapted from [29]).

of the inhomogeneous distribution of electrons of the fiber due to its amorphous structure. This electron distribution causes the refractive index to be non-uniform across the length of the fiber. As a result, an elastic scattering occurs through propagation. On the other hand, Brillouin scattering results from the interaction of light with acoustical phonons. By the nature of this mechanism, it is an inelastic scattering, which causes a frequency shift in the scattered light. If the scattered light has more energy than the incoming light, it is called anti-Stokes; if it has less energy, it is called the Stokes component. The frequency shift is both strain and temperature-dependent in Brillouin scattering. Finally, Raman scattering results from the interaction of light with optical phonons. As opposed to Brillouin scattering, Raman scattering has a constant frequency shift of $\nu_R = 440cm^{-1}$, determined by the properties of SiO_2. However, the intensity of Raman scattered light depends on the temperature, which sets the ground for temperature sensing.

Another important phenomenon in fiber optical systems is nonlinear effects. At

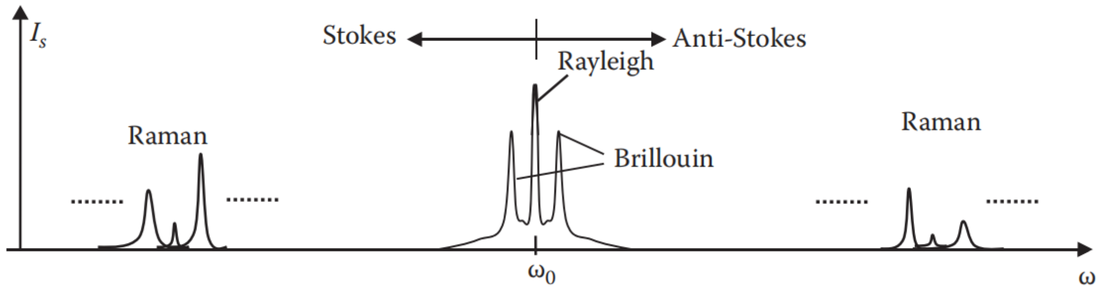

Figure 2.4: Scattered light spectrum in a conventional SMF (Adapted from [30]).

high peak powers, the optical response of the fiber is no longer linear with respect to light intensity I_0. Depending on the application, these nonlinear effects can be desired or avoided. For example, there are lasers that use Kerr nonlinearity for ultrafast pulse generation; modulation instability can be used in supercontinuum generation; by balancing the GVD and Kerr nonlinearity, an optical soliton can be generated; an entangled photon pair can be generated by spontaneous parametric down-conversion (SPDC) using a BBO crystal.

There are DFOS systems that also make use of nonlinear effects. As an example, Brillouin optical time-domain analysis-based strain sensing (BOTDA DSS) systems launch a probe signal from one end of the fiber and a pump signal from the other end of the fiber. The system then analyzes stimulated Brillouin scattering (SBS) gain through the length of the fiber. However, in the context of RDTS, the nonlinear effects must be mitigated, which are mainly modulation instability and stimulated Raman scattering (SRS). The latter sections provide prerequisites before getting into RDTS technology.

2.1 Nonlinear Schrödinger Equation

Understanding light propagation inside an optical fiber requires an engagement with Maxwell's equations that eventually leads to the derivation of the wave equation. Incorporating nonlinear polarization into this framework results in a new form of the wave equation, known as *Nonlinear Schrödinger equation* (NLSE).

This expression offers great insight into both linear and nonlinear optical phenomena during the propagation of light inside an optical fiber. To begin with, we should recall Maxwell's equations.

$$\vec{\nabla} \cdot \vec{D}(r,t) = \rho_f \tag{2.4}$$

$$\vec{\nabla} \cdot \vec{B}(r,t) = 0 \tag{2.5}$$

$$\vec{\nabla} \times \vec{E}(r,t) = -\frac{\partial \vec{B}(r,t)}{\partial t} \tag{2.6}$$

$$\vec{\nabla} \times \vec{H}(r,t) = J_f + \frac{\partial \vec{D}(r,t)}{\partial t} \tag{2.7}$$

where ρ_f and J_f are free charge density and free current density, respectively. However, we are studying dielectric materials; thus, $\rho_f = J_f = 0$. For most of the time, the electromagnetic field interacts with electrons rather than protons or nuclei. The influence of bound charges is incorporated within the definitions of $\vec{D}$ and $\vec{H}$. For the time being, let us consider only linear effects.

$$\vec{D}(r,t) = \epsilon_0 \vec{E}(r,t) + \vec{P}(r,t) \qquad \vec{H}(r,t) = \frac{1}{\mu_0}\vec{B}(r,t) - \vec{M}(r,t) \tag{2.8}$$

Recall that $\vec{M} = 0$ for dielectrics. Thus, the simplified Maxwell's equations for the following context of this discussion is as follows:

$$\vec{\nabla} \cdot \vec{D}(r,t) = 0 \tag{2.9}$$

$$\vec{\nabla} \cdot \vec{B}(r,t) = 0 \tag{2.10}$$

$$\vec{\nabla} \times \vec{E}(r,t) = -\frac{\partial \vec{B}(r,t)}{\partial t} \tag{2.11}$$

$$\vec{\nabla} \times \vec{H}(r,t) = \mu_0 \frac{\partial \vec{D}(r,t)}{\partial t} \tag{2.12}$$

With this simplified form of Maxwell's equations, we can obtain the wave equation that describes light propagation inside dielectrics.

$$\vec{\nabla} \times (\vec{\nabla} \times \vec{E}(r,t)) = \vec{\nabla} \times \left(-\frac{\partial \vec{B}(r,t)}{\partial t}\right) \tag{2.13}$$

After some substitutions and algebra, the wave equation is found to be:

$$\vec{\nabla}^2 \vec{E}(r,t) - \frac{1}{c^2}\frac{\partial^2 \vec{E}(r,t)}{\partial t^2} = \mu_0 \frac{\partial^2 \vec{P}(r,t)}{\partial t^2} \tag{2.14}$$

Before proceeding further, we should understand the relation between the electric field $\vec{E}$ and polarization $\vec{P}$. It is known that light is composed of both electric and magnetic fields. The electric field of the light interacts with the bound electrons of the dielectric medium —fiber, and induces a polarization. If the light intensity is high enough, the response of bound electrons to this electric field is anharmonic. This means that bound electrons no longer follow a basic sinusoidal oscillation, but a more complex motion, which leads to new optical frequencies being generated. In fact, this is the physical origin of nonlinear optics, where the relation between $\vec{P}$ and $\vec{E}$ is no longer linear. In the presence of weak nonlinearity, we can approach this problem using a Taylor series expansion.

$$\vec{P}(r,t) = \epsilon_0 \left(\underbrace{\chi^{(1)}(r,t)\vec{E}(r,t)}_{\vec{P}_L(r,t)} + \underbrace{\chi^{(2)}(r,t)\vec{E}^2(r,t) + \chi^{(3)}(r,t)\vec{E}^3(r,t) + ...}_{\vec{P}_{NL}(r,t)} \right) \tag{2.15}$$

where $\vec{P}_L(r,t)$, and $\vec{P}_{NL}(r,t)$ stands for linear and nonlinear polarization terms, respectively. $\chi^{(i)}$ is the susceptibility, which is direction-dependent, thereby needs to be expressed using tensors. The nonlinear term can be treated as a small perturbation to the linear polarization. At this point, it is worth mentioning that while $\chi^{(2)}$ is responsible for second harmonic generation, $\chi^{(3)}$ is responsible for Kerr nonlinearity, self-phase modulation (SPM), and four-wave mixing (FWM) processes. These nonlinear effects are crucial to understand when designing an optical system.

Further analysis requires another important approximation, a.k.a *slowly varying envelope approximation*. This approximation separates the electric field into a slowly changing amplitude and a carrier wave —that oscillates fast at the optical frequency.

$$\vec{E}(r,t) = \vec{A}(r,t)e^{i(k_0 z - \omega_0 t)} \tag{2.16}$$

where $\vec{A}(r,t)$ is the slowly varying envelope. However, for simplicity, let the electric field be along $\hat{z}$ direction and drop the vector sign. Then, the approximation implies the following:

$$\frac{\partial^2 A}{\partial z^2} << k_0 \frac{\partial A}{\partial z} \tag{2.17}$$

The equation (2.17) simplifies the problem because, since the envelope is slowly varying, its higher-order spatial derivatives can be ignored, and that makes the equations much simpler. However, the scope of this chapter does not focus on a detailed derivation of the NLSE, but rather a brief overview of its physical origins. Thus, after applying these approximations and simplifying the resulting expressions, the amplitude evolution of the light propagating inside the fiber is described as follows [31]:

$$\frac{\partial A}{\partial z} + \beta_1 \frac{\partial A}{\partial t} + \frac{i\beta_2}{2} \frac{\partial^2 A}{\partial t^2} + \frac{\alpha}{2} A = i\gamma(\omega_0)|A|^2 A \tag{2.18}$$

where β_1, β_2, α, and γ stand for first-order dispersion, second-order dispersion, attenuation coefficient, and nonlinearity parameter, respectively. The nonlinearity parameter is given by [31]:

$$\gamma(\omega_0) = \frac{\omega_0 n_2}{c A_{eff}} \tag{2.19}$$

where n_2 and A_{eff} is Kerr coefficient and effective mode area of the fiber respectively. The equation (2.19) suggests that MMFs have a lower nonlinearity parameter as their effective mode area is higher than SMFs. In fact, this is the reason why MMFs have much higher nonlinear optical power threshold than SMFs.

The equation (2.18) is difficult to solve analytically in most cases. Several numerical solutions are used to understand the pulse evolution in the fiber. One of the most widely used methods is *split-step Fourier method*, which assumes that dispersive and nonlinear effects can be calculated separately, rather than simultaneously. The method solves dispersive and nonlinear effects in two separate steps, and that is the reason why it is called split-step. However, in the case of weak light intensities and broad pulses, nonlinear effects can be ignored, and equation (2.18) can be simplified to estimate dispersive effects.

Two different length definitions are made to estimate the pulse evolution during propagation:

$$L_D = \frac{T_0^2}{|\beta_2|}, \qquad L_{NL} = \frac{1}{\gamma P_0} \tag{2.20}$$

where L_D, L_{NL}, T_0, and P_0 are dispersive length, nonlinear length, initial pulse width, and initial peak power, respectively [31]. It can be seen that if the nonlinearity parameter γ is weak enough, L_{NL} approaches infinity. In that case, only the dispersive effects control the pulse evolution. However, at high peak powers, the nonlinear length gets smaller. If L_{NL} is smaller than the length of the fiber L, nonlinear effects start to accumulate after a propagation distance of L_{NL}. The ratio of L_D/L_{NL} is a good measure to determine whether the pulse evolution is mostly influenced by dispersive or nonlinear effects.

$$\frac{L_D}{L_{NL}} << 1, \qquad\qquad \frac{L_D}{L_{NL}} >> 1 \tag{2.21}$$

If the ratio is much less than 1, dispersive effects are dominant, but if the ratio is much greater than 1, nonlinear effects are dominant. Therefore, it can be concluded that the pulse evolution depends on the pulse width and peak power.

For the consideration of pulse propagation in an optical fiber, second-harmonic generation is not allowed because second-order susceptibility $\chi^{(2)}$ is zero for amorphous crystals —such as SiO_2. However, every material has a non-zero third-order susceptibility $\chi^{(3)}$, because it is not forbidden by inversion symmetry, making third-order nonlinear effects allowed in both centrosymmetric and non-centrosymmetric media. In fact, it is the most important term in explaining nonlinear effects, as it causes many of them: Kerr nonlinearity, FWM, SPM, cross-phase modulation (XPM). Third-order polarization due to $\chi^{(3)}$ is expressed as follows:

$$\begin{aligned}
P^{(3)}(t) &= \epsilon_0\chi^{(3)}E^3(t) \\
&= \epsilon_0\chi^{(3)}\left(\frac{1}{2}\tilde{E}e^{i\omega t}\right)^3 \\
&= \frac{1}{8}\epsilon_0\chi^{(3)}(\tilde{E}e^{i\omega t}+\tilde{E}^*e^{-i\omega t})(\tilde{E}e^{i\omega t}+\tilde{E}^*e^{-i\omega t})(\tilde{E}e^{i\omega t}+\tilde{E}^*e^{-i\omega t}) \\
&= \frac{1}{8}\epsilon_0\chi^{(3)}\left(\underbrace{\tilde{E}^3e^{3i\omega t}+\tilde{E}^{*3}e^{-3i\omega t}}_{\text{third harmonic}}+\underbrace{3\tilde{E}(\tilde{E}\tilde{E}^*)e^{i\omega t}+3\tilde{E}^*(\tilde{E}\tilde{E}^*)e^{-i\omega t}}_{\text{self phase modulation}}\right)
\end{aligned} \tag{2.22}$$

where $\tilde{E}$ is used for the Fourier transformed electric field. From equation (2.22), it is seen that there is intensity dependency in the SPM term. This intensity dependency appears in the nonlinear dielectric constant as well. Below equation presents the nonlinear dielectric constant due to $\chi^{(3)}$:

$$\epsilon_{NL}(t) = \frac{3}{4}\chi^{(3)}|E(t)|^2 \tag{2.23}$$

This nonlinear term contributes to the overall dielectric constant of the material as follows:

$$\epsilon(\omega) = 1 + \chi^{(1)} + \epsilon_{NL} \tag{2.24}$$

Notice that the above expression is in the Fourier domain. The result of this nonlinear dielectric constant contribution manifests itself as an intensity-dependent refractive index $\tilde{n}$ in the fiber.

$$\tilde{n} = n + \underbrace{\tilde{n_2}|E|^2}_{\Delta n} \tag{2.25}$$

where Δn is the change in refractive index due to nonlinearity, and $\tilde{n}_2$ is the intensity-dependent refractive index, which is described as follows:

$$\tilde{n}_2 = \frac{3}{8n}Re\{\chi^{(3)}\} \tag{2.26}$$

As a result of this intensity-dependent refractive index, light gets a phase shift during propagation, eventually leading to a spectral broadening. This phenomenon is widely used in ultrashort pulse generation.

Another consequence of SPM is the modulation instability (MI). MI can simply be explained as the amplification of noise. Consider a quasi-continuous wave optical pulse with $\tau_p = 100ns$ pulse duration. There certainly is noise accompanying the pulse, such as amplified spontaneous emission (ASE), or even something more fundamental: vacuum fluctuations. Let the noise be treated as a perturbation to the steady state solution of the optical pulse. Consider a perturbation frequency of $\pm\Omega$. Then, due to the nonlinear phase shift caused by SPM, new optical frequencies are generated at $\pm\Omega$, which turn out to be spectral sidebands of MI. The physical process behind MI is that photons in the probe pulse are annihilated to create new photons corresponding to the gain spectrum of MI. This process is actually known as four-wave mixing (FWM) and is phase-matched by SPM. It should be noted that due to the phase-matching condition, MI occurs in the anomalous GVD region ($\beta_2 < 0$). The result of this phenomenon in an RDTS system is a reduction in probe power, followed by a reduction in the SNR.

In most applications, dispersive effects are inevitable. In the context of RDTS, pulse broadening in the time domain due to GVD causes deterioration of spatial resolution at further distances. On the other hand, modal dispersion limits the sensing distance of an MMF. MI is also a limiting factor as it reduces the probe power. Another important nonlinear phenomenon that limits the performance of RDTS is stimulated Raman scattering (SRS). In fact, Raman scattering is also a nonlinear effect. However, it does not happen instantaneously as opposed to other nonlinear effects. Thus, Raman scattering is referred to as *delayed nonlinear effect*. The details of Raman scattering are explained in the next part of this chapter.

2.2 Raman Scattering

Light-material interactions come in various ways: light absorption, emission, and scattering. Each of these phenomena can be harnessed to create technologies, such as perfect light absorbers used in energy harvesting [32], laser or LED sources. In the context of RDTS, the primary light-material interaction is Raman scattering, which occurs due to molecular vibrations of the material, *a.k.a.* optical phonons.

The key principle behind Raman scattering is that an incoming photon excites the electron of the material to a virtual state. Virtual states do not correspond to real, discrete quantum states of the material, but rather a term referring to the perturbation of the electrons. As a result, the electrons do not make discrete state transitions. This kind of absorption is often called virtual absorption, and this process does not conserve energy [33]. Due to virtual absorption, the incoming photon annihilates. If an optical phonon also annihilates during the scattering process, its energy is contributed to the incoming photon; thus, the scattered photon has increased energy. This scattered light is referred to as Raman anti-Stokes light. On the other hand, if the annihilated photon loses some of its energy into the creation of an optical phonon, the scattered light has decreased energy and is known as Raman Stokes light. This process is known as spontaneous Raman scattering, with the following relations:

$$\omega_{as} = \omega_0 + \omega_{fi} \tag{2.27}$$

$$\omega_s = \omega_0 - \omega_{fi} \tag{2.28}$$

where $\omega_{as,s}$ are the frequency of anti-Stokes and Stokes respectively, ω_0 is the frequency of incoming photon, and ω_{fi} is the frequency shift due to Raman scattering. Due to this frequency shift, Raman scattering is inelastic in nature. The resulting anti-Stokes and Stokes wavelengths for a probe wavelength of λ_0 are given as follows [10]:

$$\lambda_{as} = \frac{0.01}{\frac{0.01}{\lambda_0} + \nu_R}, \qquad \lambda_s = \frac{0.01}{\frac{0.01}{\lambda_0} - \nu_R} \tag{2.29}$$

where ν_R is the frequency shift due to Raman scattering. The amount of frequency shift depends on the fiber material. For SiO_2, frequency shift is given as $\nu_R = 440cm^{-1}$. In this thesis, the conventional telecom wavelength $\lambda_0 = 1550nm$ is used for the probe. Thus, the corresponding anti-Stokes and Stokes wavelengths are $\lambda_{as} = 1450$, and $\lambda_s = 1660$. These wavelengths are the signals of interest at the receiver end. The latter discussion presents the temperature dependency of Raman scattering phenomena. However, it is shown in the Figure 4.4g that stimulated Raman scattering occurs at high peak powers and should be avoided.

2.2.1 Temperature Dependency of Raman Scattering

Due to the fact that optical phonons are temperature dependent, so is the Raman scattering. The scattered Raman intensity is given as follows as a function of temperature:

$$I_{as}(T) = \frac{K_{as}}{\lambda_{as}^4} \frac{1}{exp\left(\frac{h\nu_R c}{k_b T}\right) - 1}, \quad I_s(T) = \frac{K_s}{\lambda_s^4}\left[\frac{1}{exp\left(\frac{h\nu_R c}{k_b T}\right) - 1} + 1\right] \tag{2.30}$$

where $K_{as,s}$ are Raman scattering coefficients related to Raman cross-section, h, c, and k_B are Planck's constant, speed of light in free space, and the Boltzmann constant [10]. However, it is more convenient to use their ratio in RDTS systems. Figure 2.5 shows the scattered Raman intensity and their ratio as a function of temperature. It should be noted that the figure is normalized to $K_{as}/\lambda_{as}^4 = 1$, and $K_s/\lambda_s^4 = 1$ respectively [10].

$$R(T) = \frac{I_{as}(T)}{I_s(T)} = \frac{K_{as}}{K_s}\left(\frac{\lambda_s}{\lambda_{as}}\right)^4 exp\left(-\frac{h\nu_R c/k_B}{T}\right) \tag{2.31}$$

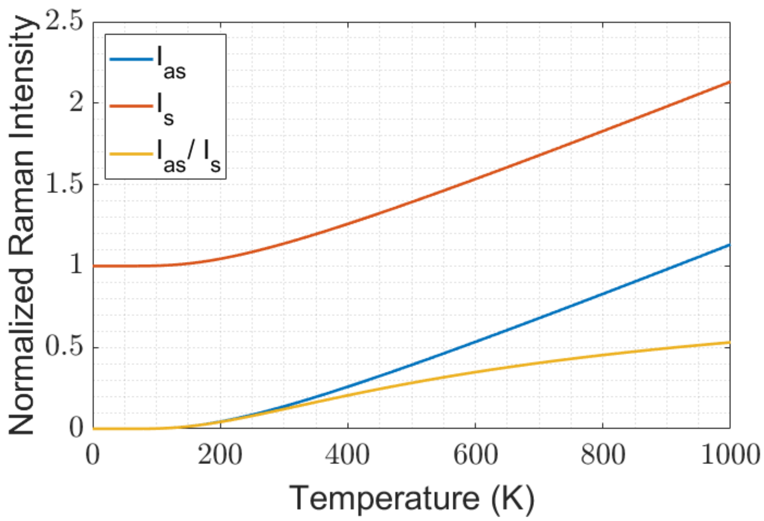

Figure 2.5: Raman scattering as a function of temperature.

From the figure, it is shown that the Raman ratio $R(T)$ is not linear. However, at temperatures between $200 - 400K$, the graph looks relatively linear. The importance of this is that the temperature sensitivity reduces at very high temperatures, and the demodulation becomes more difficult. Based on this temperature dependency, the temperature of the environment in which the fiber is placed can be spatially resolved by implementing the OTDR principle. The following section discusses the OTDR principle.

2.3 OTDR Principle

The majority of the optical fibers are located under the soil and oceans, which makes them difficult to perform maintenance and repair. However, a technique called *optical time-domain reflectometry (OTDR)* allows for the precise location of fiber faults for easier maintenance and repair. The technique is primarily based on sending a pulse of light into the fiber and receiving the backscattered Rayleigh light at every position along the length of the fiber.

The OTDR technique resembles the working principle of a radar. While radar sends an RF signal to free space and receives an echo from an object, OTDR does it in a fiber environment using an optical pulse, and instead of measuring the echo signal, it measures scattered light. By measuring the Rayleigh scattered light, bend induces losses, splice losses, and fiber break points can be identified.

DFOSs are mostly based on the OTDR principle —there are DFOSs based on optical-frequency-domain reflectometry (OFDR) as well. In the context of RDTS, OTDR is responsible for measuring and ranging the temperature-dependent Raman backscattered light. However, it is important to understand the performance metrics of an OTDR, such as spatial resolution, interrogation period, and measurement range. The discussion is followed by a brief explanation of these performance metrics in consideration of RDTS.

Spatial Resolution In an OTDR system, the ability to distinguish two neighboring scattering events is referred to as spatial resolution (SR). If any two neighboring events are closer than SR to each other, the OTDR cannot distinguish them. SR is mainly determined by pulse duration. An optical pulse illuminates the fiber as follows:

$$W = \frac{c\tau_p}{n_f} \tag{2.32}$$

where W, c, τ_p, and n_f denote the spatial width of the pulse, speed of light in free-space, pulse duration, and refraction index of the fiber, respectively. The dimensions of W are meters, and it corresponds to the illuminated part of the fiber. For typical values of $\tau = 100ns$, and $n_f = 1.46$, spatial width becomes $W \approx 20m$. When the pulse experiences GVD, it gets broader in the time domain, as a result, SR deteriorates at longer distances.

Interrogation Period The interrogation period is the time it takes to launch the next optical pulse for the subsequent interrogation of the fiber. As meaningful as it seems to increase the repetition rate of the pulses, there is a limit to that. Due to the length of the fiber, there exists a waiting time before launching a new optical pulse. Otherwise, the optical pulse and backscattered light would overlap with each other, and the ranging would not be possible. The interrogation period is given as follows:

$$\tau_i = \frac{2Ln_f}{c} \tag{2.33}$$

where τ_i, L are the interrogation period and the length of the fiber, respectively. The factor of 2 stands for round-trip distance. Consider a sensing fiber of $L = 10km$, with $n_f = 1.46$, the interrogation period becomes $\tau_i \approx 100\mu s$. Thus, each subsequent pulse must be launched at this period. The reciprocal of τ_i defines the repetition rate as follows:

$$f_r = \frac{1}{\tau_i} \tag{2.34}$$

For an interrogation period of $100\mu s$, the repetition rate is $f_r = 10kHz$. Repetition rate also determines the measurement bandwidth of the system. Sampling at a rate of $10kHz$ yields a measurement bandwidth of $5kHz$ due to the Nyquist sampling theorem. However, measurement bandwidth is a more important metric for acoustical sensing. In the context of RDTS, it is not very crucial.

Measurement Range The measurement range is the maximum distance at which the OTDR can perform. It is mentioned that Raman scattering is the weakest scattering mechanism among others. As a result, increasing the measurement range is a big challenge in RDTS technology. The measurement range is related to the optical power launched into the sensing fiber, as well as the sensitivity of the APDs used. The backscattered Raman anti-Stokes and Stokes powers are given as follows:

$$P_{as}(z) = P(0)\eta_{as}(z)exp\left(-\int_0^z(\alpha_p(z') + \alpha_{as}(z'))dz'\right) \tag{2.35}$$

$$P_s(z) = P(0)\eta_s(z)exp\left(-\int_0^z(\alpha_p(z') + \alpha_s(z'))dz'\right) \tag{2.36}$$

where $P(0)$ is the initial power at $z = 0$; $\eta_{as,s}$ are the backscatter factor for each Raman component; α_p and $\alpha_{as,s}$ are the attenuation coefficients at the probe, anti-Stokes and Stokes wavelengths respectively [10]. In the above equations, $\eta_{as,s}$ takes into account the power that is converted from probe to Raman components due to scattering.

$$\eta_{as}(z) = \frac{1}{2}\alpha_{ras}(z)\nu_{g_{as}}B_{as}(z) \tag{2.37}$$

$$\eta_s(z) = \frac{1}{2}\alpha_{rs}(z)\nu_{g_s}B_s(z) \tag{2.38}$$

where $\alpha_{ras,rs}$ stands for the attenuation in the probe power due to Raman scattering at the anti-Stokes and Stokes wavelengths, respectively. $\nu_{g_{as,s}}$ are the group velocity at respective Raman scattered wavelengths. Whereas $B_{as,s}$ are the capture fractions at respective wavelengths [10]. As a result of these attenuation mechanisms, the power of each Raman component falls below the detectable power level of the APDs at further distances. Optimizing the optical power without experiencing nonlinearities, implementing advanced denoising techniques, and pulse coding methods allows longer measurement ranges to be achieved. The next section discusses noise sources and Wavelet denoising.

2.4 Distributed Temperature Sensing

Distributed temperature sensing (DTS) using optical fibers offers a unique and powerful solution for real-time, spatially resolved thermal monitoring over long distances. Unlike conventional point sensors that provide localized data, DTS systems utilize the optical fiber itself as a continuous sensing element, capable of detecting temperature variations at every point along its length.

The core principle behind Raman OTDR-based DTS systems is the interaction of light with molecular vibrations in the optical fiber, specifically Raman scattering. As introduced in Chapter 2, Raman scattering gives rise to two components: Stokes and anti-Stokes signals. The anti-Stokes component exhibits a stronger temperature dependency and is thus primarily used in temperature demodulation.

The fiber is interrogated by a short optical pulse, and the backscattered Raman signals are measured as a function of time. This time-resolved signal is then mapped to the physical location along the fiber using the known group velocity of light in the fiber. The measured intensities of the anti-Stokes and Stokes components are used to calculate the temperature via a demodulation scheme. There are two main demodulation schemes used in the literature: single-channel demodulation and dual-channel demodulation. Whereas single-channel demodulation focuses solely on the Raman anti-Stokes component to retrieve the temperature information, the dual-channel demodulation method utilizes both the Raman Stokes and anti-Stokes components. Figure 2.6 shows an experimental setup used for single-channel demodulation. The experimental setup consists of only one APD and amplifier, which reduces the complexity and cost of the system. However, since this method is solely based on the anti-Stokes component, it is strictly sensitive to power fluctuations of the laser light and attenuation profile of the sensing fiber. As a result, single-channel demodulation offers limited accuracy as well as reduced robustness over long operational periods. For that reason, dual-channel demodulation is used dominantly in the literature. As this thesis uses a dual-channel demodulation scheme, only the details of dual-channel demodulation are explained in this chapter.

Regarding system design, DTS systems can be used as single-ended or in a loop configuration. While only one end of the sensing fiber is connected to the DTS unit in a single-ended configuration, two ends of the sensing fiber are both connected in the latter case. Figure 2.6 illustrates the loop configuration. The two ends of the sensing fiber are connected to an optical switch, as shown in the experimental setup. The system interrogates two ends of the fiber by switching light from one end to the other, which doubles the measurement time. Although

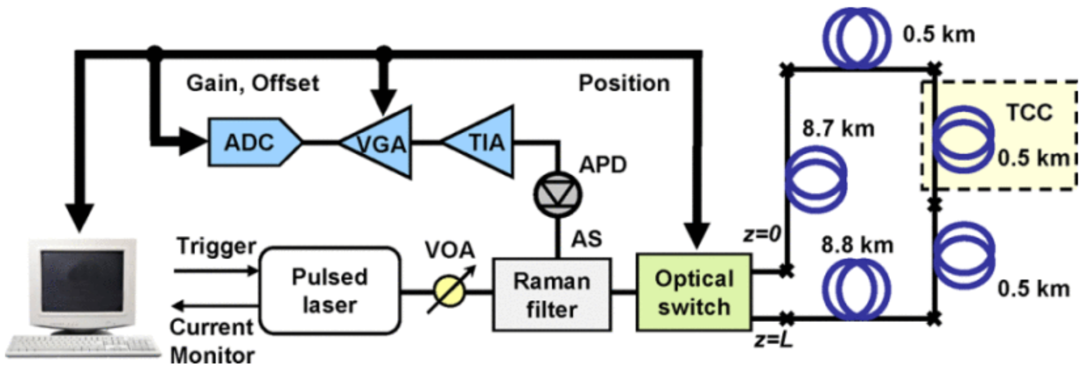

Figure 2.6: Loop configuration and single-channel demodulation experimental setup (Adapted from [34]).

the loop configuration allows for higher SNR than a single-ended configuration, there are a few setbacks; the measurement time increases due to doubled interrogation, and the system cannot continue monitoring the temperature if the fiber is broken. However, the system complexity of the single-ended configuration is less than that of the loop configuration, and it can keep the temperature monitoring until the fiber fault location. In this thesis, the single-ended configuration is used.

Dual-channel demodulation utilizes both the anti-Stokes and Stokes components of the Raman backscattered signal to enhance the accuracy and stability of temperature measurements. As shown in Equations 2.36 and 2.38, the detected signals depend on several system parameters, including the input pulse energy, the optical capture fraction, and attenuation at the probe wavelengths. However, by taking the ratio of the anti-Stokes to Stokes intensities, many of these system-dependent variables cancel out. This leads to a simplified and more robust temperature demodulation approach, which can be described by the following relation:

$$R(T(z)) = \frac{K_{as}}{K_s}\left(\frac{\lambda_s}{\lambda_{as}}\right)^4 exp\left(-\frac{S_{LE}}{T(z)}\right) exp\left(-\int_0^z (\alpha_{as}(z') - \alpha_s(z'))dz'\right) \quad (2.39)$$

Where λ_{as}, λ_s are Raman anti-Stokes, and Stokes wavelengths respectively; K_{as}, K_s are Raman scattering coefficients for respective wavelengths; S_{LE} is a fiber specific parameter —depends on the fiber material; α_{as}, α_s are loss coefficients for respective wavelengths [10]. The integral term in equation 2.39 accounts for differential attenuation throughout the sensing fiber. However, further system-dependent parameters due to photodetector sensitivity, transmission of the Raman Wavelength Division Multiplexer (WDM), or the Raman scattering coefficients K_{as} and K_s cannot be directly measured and compensated with great precision. Instead, a calibration method is needed to mitigate the uncertainties in these parameters. Calibration typically involves exposing a known section of the fiber, called the reference fiber —or reference coil —to a known temperature environment. The temperature of the reference coil is typically measured using a point sensor. The DTS system is then adjusted so that the measured signal corresponds to the actual known temperature of the reference coil. The equation 2.39 then takes a new form as follows:

$$\tilde{R}(T(z)) = \frac{R(T(z))}{R(T(rc))} = exp\left(S_{LE}\left(\frac{1}{T_{ref}} - \frac{1}{T(z)}\right)\right) exp\left(-\int_{z_{ref}}^{z} (\alpha_{as}(z') - \alpha_s(z'))dz'\right) \tag{2.40}$$

where $R(T(rc))$ is the Raman ratio of the distance from the beginning of the fiber to the end of the reference coil [10]. After the calibration, temperature can easily be retrieved as follows [10]:

$$\frac{1}{T(z)} = \frac{1}{T_{ref}} - \frac{1}{S_{LE}}\left(ln(\tilde{R}(z)) + \int_{z_{ref}}^{z} (\alpha_{as}(z') - \alpha_s(z'))dz'\right) \tag{2.41}$$

In addition to dual-channel demodulation and this simple calibration scheme, novel demodulation and calibration schemes are suggested in the DFOS literature. In 2010, Hwang et al. reported a self-calibration scheme to increase temperature accuracy by using an end-reflector [35]. In 2023, Li et al. reported a chaotic correlation demodulation scheme using a chaotic laser to improve the spatial resolution of RDTS systems [23]. Their results showed that chaotic correlation demodulation scheme can provide a spatial resolution independent of the pulse duration.

DTS systems efficiently monitor temperature profiles across large infrastructures, leveraging the inherent advantages of optical fibers. Dual-channel demodulation, supported by robust calibration, enables high-resolution and high-accuracy measurements. However, the inherently low signal levels of Raman scattering still pose a challenge for long-range sensing. The next chapter addresses this limitation by introducing Simplex coding, a pulse modulation technique that significantly improves the SNR without compromising spatial resolution.

2.5 Measurement Noise

In RDTS systems, accurate temperature demodulation is critically dependent on the quality of the backscattered signal. However, the inherently weak nature of Raman scattering, as well as attenuation over distance, combined with several sources of noise, affects the system's performance. Understanding and mitigating these noise components is essential for enhancing the SNR, increasing sensing range, and improving temperature resolution. Before going further, the following definition of SNR should be recalled:

$$SNR = \frac{P_{signal}}{P_{noise}} \tag{2.42}$$

Where P_{signal} and P_{noise} are the power of the signal and noise, respectively. However, using a logarithmic scale is more convenient than a linear scale, as it makes it easier to distinguish between two adjacent values that would otherwise appear very close together in a linear representation. Thus, SNR is usually described in dB as follows:

$$SNR_{dB} = 10log_{10}\left(\frac{P_{signal}}{P_{noise}}\right) \tag{2.43}$$

The primary sources of measurement noise in RDTS systems are photon shot noise, thermal noise, amplifier noise, and background light noise. Photon shot noise arises due to the statistical nature of light [36] and is more pronounced in systems operating under low-light conditions, as is typical with anti-Stokes signal detection. Thermal noise originates from the random motion of electrons in electronic components [37]. Photodetectors are often characterized by their noise equivalent power (NEP). NEP refers to power generated by a photodetector due to a noise source [38]. It is a measure of photodetector sensitivity, which is given as $W/\sqrt{Hz}$. A lower NEP allows for the detection of weaker optical signals.

Thermal noise in an avalanche photodiode (APD) generates a current, thus contributing to the ground noise of the APD. Surface leakage current and shot noise also contribute to the ground noise of the APD. The ground noise depends on the operating temperature of the APD. As a result, ground noise dynamically changes. In 2019, Yan et al. suggested a dynamic difference noise algorithm to overcome this issue [12]. They basically measure the noise floor of the APD in each interrogation and subtract it from the Raman signal.

In addition, background light, such as unfiltered Rayleigh backscattered signal entering the detection path, can introduce additional noise and distort the measurement. In 2013, Sun et al. estimated the Rayleigh noise by placing two reference fibers at different temperatures [39]. Their results showed that the Raman anti-Stokes channel is occupied by the Rayleigh signal by an amount of 15%.

The dominant noise in RDTS systems is thermal noise, which is categorized as additive white Gaussian noise (AWGN). AWGN has zero mean value, and is random with a Gaussian distribution [40]. It is referred to as “white” noise because its power spectral density is uniform across the frequency domain. The most common and easiest method to suppress this noise is to take the algebraic average of consecutive measurements. However, this increases the overall measurement time and can be impractical for certain areas. For example, RDTS systems made for fire detection are supposed to generate a fire alarm in a few seconds [41]. Long averaging durations are a limiting factor in this case. To overcome this limitation, advanced denoising algorithms are used.

Among various noise suppression techniques, digital denoising is desired because it does not increase the system complexity, as well as the cost. In this thesis, wavelet transformation-based denoising is performed. This method was demonstrated in 2015 by Saxena et al. in RDTS systems [42]. Wavelet denoising effectively suppresses the AWGN and can reduce the total measurement time of an RDTS system with no additional cost. The latter section explains the wavelet denoising.

2.5.1 Wavelet Denoising

Many digital denoising algorithms are based on the Fourier transformation, as it is generally easier to work in the frequency domain. They are widely used in image and video denoising, audio denoising, denoising of medical signals [43], and beyond. In addition, modified versions of the Fourier transformation are also used, such as short-time Fourier transformation (STFT) and continuous wavelet transformation (CWT). Whereas STFT uses a window function, CWT uses a basis function called *mother wavelet*.

$$F(\omega) = \int_{-\infty}^{\infty} f(t)e^{i\omega t}dt \tag{2.44}$$

Equation 2.44 defines the Fourier transformation, where $f(t)$ is the signal measured in the time domain. The Fourier transformed signal $F(\omega)$ is analyzed in the frequency domain. Low-pass, high-pass, or band-pass filters are typically used for signal denoising in the frequency domain. However, these filters are not optimized for dynamically changing noise sources. The signals of interest in RDTS, Raman anti-Stokes and Stokes, are considered to be nonstationary by their nature [44]. Because the information about time is completely lost after Fourier transformation, it can be difficult to analyze the signal without that knowledge in some other applications as well, such as monitoring of seismic activities [45], and for certain radar signals [46] which needs to be analyzed with knowledge in time and frequency domain both. In the context of RDTS, implementation of Fourier transformation-based denoising schemes can introduce degradation of spatial resolution, and an ambiguity of locating the hot zones in the sensing fiber [47]. To overcome this limitation, the STFT method can be used, which preserves both the time and frequency information of a signal. To achieve that, it uses a window function $w(t-\tau)$ during the transformation process as shown in equation 2.45.

$$F(\tau,\omega) = \int_{-\infty}^{\infty} f(t)w(t-\tau)e^{i\omega t}dt \tag{2.45}$$

The window function captures the fraction of a signal that corresponds to the given window duration. It achieves this by sliding the window function by an amount of τ. Therefore, τ is called the shifting or sliding parameter. However, there is an uncertainty principle between time and frequency as follows:

$$\Delta t \Delta f \geq \frac{1}{4\pi} \tag{2.46}$$

The higher the resolution in the time domain, the lower the resolution in the frequency domain, or vice versa. Figure 2.7 shows the time and frequency resolution of STFT on the left side.

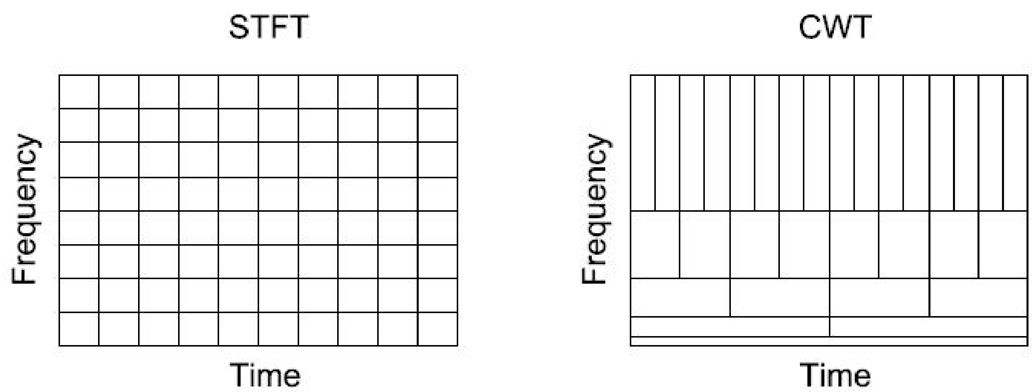

Figure 2.7: Time and frequency resolution of STFT and CWT (Adapted from [48]).

As seen from the figure above, the STFT method has a fixed resolution for every frequency value. But a denoising algorithm based on this method can disturb the signal integrity due to this fixed resolution. However, the analysis can be improved with a multi-resolution approach. Since the low-frequency component of a signal varies slowly over time, they don't need a high resolution in the time domain, but a high resolution in the frequency domain. Likewise, the high-frequency component of a signal varies rapidly over time. As a result, they need higher resolution in the time domain [49]. This multi-resolution analysis is possible by CWT, and was first suggested by Mallat et al. in 1989 [50]. As shown in equation 2.47, the window function is replaced by a new function $\psi\left(\frac{t-\tau}{s}\right)$.

$$F(\tau, s) = \frac{1}{|s|} \int_{-\infty}^{\infty} f(t) \psi\left(\frac{t-\tau}{s}\right) e^{i\omega t} dt \tag{2.47}$$

$F(\tau, s)$ is the wavelet coefficient, where s is the scaling factor which defines the frequency equivalent of the mother wavelet as follows:

$$s \equiv \frac{1}{f} \tag{2.48}$$

Similar to STFT, the mother wavelet captures the fraction of a signal that corresponds to the given wavelet. However, as opposed to a window function —which just has a time dependency —the mother wavelet has both time and frequency properties. While the shifting parameter τ captures the temporal characteristics of a signal, the scaling factor s captures the frequency characteristics. Due to this property, CWT allows a multi-resolution analysis as shown on the right side of the Figure 2.7. In a sense, a mother wavelet (will be called wavelet hereinafter) is like a sinusoidal, but localized in time with certain shapes; Haar, Mexican hat, Daubechies, etc. Figure 2.8 shows various wavelet types, where "db" stands for Daubechies.

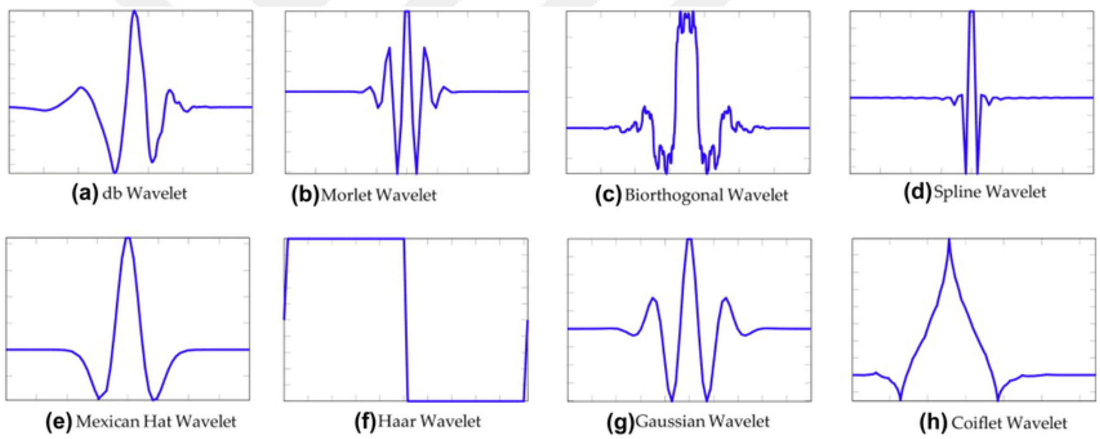

Figure 2.8: Wavelet family (Adapted from [51]).

After the transformation, wavelet coefficients $F(\tau, s)$ are evaluated based on a denoising algorithm. The algorithm uses a thresholding mechanism. Coefficients larger than a threshold are considered to belong to the signal itself, those lower than the threshold are considered to belong to the noise [42]. Multi-resolution analysis decomposes the signal into low-frequency and high-frequency components, which are called the approximation and detail of that signal, respectively. Approximations are considered to be useful for retrieving the clean signal [52].

Choosing the proper type of wavelet is important, as they have different properties: smoothness, vanishing moments, and orthogonality. Wavelet transformation is not only used for signal denoising, but also for pattern recognition [53], data compression [54], and feature detection [55]. Therefore, their properties are thoroughly explored for various applications. For the purpose of signal denoising, orthogonal wavelets are more effective than non-orthogonal ones. The higher the similarity between the shape of the wavelet and the signal, the better the signal denoising [56]. Ershov et al. experimentally demonstrated DWT denoising in RDTS systems with Daubechies wavelet —orthogonal —for their convenience for low SNR signals [57]. Therefore, due to their effectiveness, the Daubechies type of wavelet is used in this thesis for the denoising process.

In this thesis, the MATLAB environment is used for data analysis, as well as wavelet denoising. Table 2.1 shows the MATLAB parameters used for wavelet denoising. It is important to mention that CWT is computationally demanding, thus, it takes too much time. For this reason, discrete wavelet transformation (DWT) is performed for denoising.

Wavelet type	db2
Denoising method	Minimax
Threshold rule	Soft
Noise estimate	Level independent

Table 2.1: Matlab parameters for wavelet denoising.

Daubechies wavelets are named as "*dbN*" where N is the order of the wavelet. $db1$ is known as a Haar wavelet and is the simplest form of existing wavelets. It is good at recognizing discontinuities in a signal. That is because the Haar wavelet itself is considered to be a discontinuous wavelet function. For that reason, $db1$ or Haar wavelet does not perform well at denoising Raman anti-Stokes and Stokes signals. Instead, $db2$ is chosen as the wavelet.

Chapter 3

Simplex Coding Technique

As mentioned earlier, the SNR of an RDTS system is inherently limited due to the weak nature of Raman scattering —on the order of nanowatts. Additionally, optical nonlinearities impose a constraint on the peak power of optical pulses. Although increasing the pulse duration can improve the pulse energy, it comes at the cost of degraded spatial resolution. To overcome these limitations, an advanced interrogation technique known as pulse coding is employed. Instead of using a single optical pulse per interrogation cycle, this method spreads a sequence of optical pulses in the time domain, according to a predetermined codeword. By utilizing multiple pulses within each cycle, pulse coding effectively suppresses the uncorrelated AWGN (additive white Gaussian noise), thereby enhancing the SNR. Decoding the measured OTDR traces using a certain set of rules —provided by the pulse coding scheme —, and demodulating the decoded traces enables temperature sensing over longer distances.

Various pulse coding techniques are derived from established mathematical structures, including Hadamard matrices, complementary codes [58], and orthogonal codes. Over time, coding schemes like pulse compression, linear combination, and correlation-based codes have been widely adopted in diverse applications, including LiDAR [59], radar [60], ultrasonic testing [61], steganography [62], and code-division multiple access (CDMA) systems [63].

Depending on the application, the pulse coding technique can be implemented in various modulation schemes, e.g., amplitude modulation, phase modulation, and frequency modulation. However, in the context of RDTS, pulses are amplitude modulated based on a codeword. The most common pulse coding techniques in the DFOS literature are Simplex (linear combination) and Golay (correlation-based) coding schemes.

Simplex coding is one of the most widely used pulse coding techniques in RDTS systems. Before its implementation into RDTS technology, it was theoretically suggested in 1993 by Jones et al. to use in OTDR systems [64]. In 2004, an analysis and an experimental demonstration in an OTDR setup is reported by Lee et al. [26]. In the following years, Bolognini et al. experimentally demonstrated Simplex coded RDTS [65]. The key idea is to interrogate multiple positions in the sensing fiber simultaneously by using more than one pulse per interrogation cycle, thus increasing the system's SNR, while maintaining the spatial resolution equivalent to that of a single pulse. To achieve this, the laser is amplitude modulated according to the codewords of the Simplex coding scheme.

The mathematical foundation of Simplex coding lies in Hadamard matrices [66], which consist of ± 1 entries and exhibit mutual orthogonality —meaning that each row vector is orthogonal to all others. This orthogonality is a crucial property in certain fields of optics, e.g., optical communication systems, as it reduces signal interference. A well-known application of orthogonal codes is CDMA, where a low correlation between codewords helps to minimize cross-talk, as well as allows an increase in the number of users in the communication channel [67].

In digital coding schemes, a code that consists of ± 1 values is said to be *bipolar*. However, in amplitude modulation of light, -1 does not have a physical meaning in terms of optical power. Therefore, Hadamard matrices must be converted into *unipolar* form with binary values of 0 and 1, where the bit states 0 and 1 correspond to the laser being off and on, respectively.

To construct a Simplex code, the Hadamard matrix H_{2^n} of order 2^n is first converted to a unipolar form by replacing the elements of -1, and 1 with 1, and 0, respectively. Notice that the first row and column of any Hadamard matrix contain only 1s, which means the laser is not being amplitude modulated as the bit state is always 1. Thus, removing the first row and column results in a new matrix of order $2^n - 1$, whose row vectors define the Simplex codes. The number of bits in a Simplex code is called the *code length* L, and is equal to the order of the matrix.

$$L \equiv 2^n - 1 \tag{3.1}$$

Each row of the Simplex code is referred to as *codeword*, which is used for different interrogations. Since the Simplex code matrix is square, the number of codewords is equal to the code length L. This means that for a Simplex code of length L, there are L different OTDR traces obtained from each codeword. The obtained traces are linear superpositions of the single pulse response of each optical pulse within the codeword. Therefore, a decoding process is required to obtain the single pulse response of the system. The decoding process is achieved by multiplying the OTDR traces by the inverse Simplex matrix S^{-1}. In the latter sections, an SNR comparison of Simplex coding with traditional single pulse interrogation is discussed.

3.1 Constructing the Simplex Codes

To construct a Simplex code, one must start with a Hadamard matrix H_{2^n} of order 2^n. Let $n = 2$ for the sake of simplicity.

$$H_4 = \begin{bmatrix} 1 & 1 & 1 & 1 \\ 1 & -1 & 1 & -1 \\ 1 & 1 & -1 & -1 \\ 1 & -1 & -1 & 1 \end{bmatrix} \tag{3.2}$$

As can be seen, the first row and column of the Hadamard matrix consist of only 1s. As the bit state is always 1, there is no amplitude modulation of the laser.

Thus, the first row and column can be omitted. Let's call the newly constructed matrix H_3'.

$$H_3' = \begin{bmatrix} -1 & 1 & -1 \\ 1 & -1 & -1 \\ -1 & -1 & 1 \end{bmatrix} \tag{3.3}$$

Finally, H_3' is converted to a unipolar form simply by replacing -1 and 1 elements with 1 and 0, respectively. The resulting matrix S is the Simplex code of order $2^n - 1 = 3$, recalling that $n = 2$.

$$S = \begin{bmatrix} 1 & 0 & 1 \\ 0 & 1 & 1 \\ 1 & 1 & 0 \end{bmatrix} = \begin{bmatrix} S_1 \\ S_2 \\ S_3 \end{bmatrix} \tag{3.4}$$

where S_1, S_2 and S_3 are the codewords used in each interrogation.

3.2 Decoding of OTDR Traces

Since the interrogation contains many pulses, the measured OTDR traces are linear superpositions of the single pulse response of each optical pulse within the codeword. Let $\psi_{ijk}(t)$ denote the measured OTDR trace at time t, where i, j, and k are the bit states. Then, the coded traces are as follows;

$$\begin{bmatrix} \psi_{101}(t) \\ \psi_{011}(t) \\ \psi_{110}(t) \end{bmatrix} = \begin{bmatrix} \psi_{100}(t) + \psi_{001}(t) + e_{101}(t) \\ \psi_{010}(t) + \psi_{001}(t) + e_{011}(t) \\ \psi_{100}(t) + \psi_{010}(t) + e_{110}(t) \end{bmatrix} \tag{3.5}$$

where the term $e_{ijk}(t)$ stands for the measurement error. Here, the noise is assumed to be additive white Gaussian noise with zero mean value and variance of σ^2. After some rearrangement of equation 3.5, it becomes

$$\begin{bmatrix} \psi_{101}(t) \\ \psi_{011}(t) \\ \psi_{110}(t) \end{bmatrix} = \underbrace{\begin{bmatrix} 1 & 0 & 1 \\ 0 & 1 & 1 \\ 1 & 1 & 0 \end{bmatrix}}_{S} \begin{bmatrix} \psi_{100}(t) \\ \psi_{010}(t) \\ \psi_{001}(t) \end{bmatrix} + \begin{bmatrix} e_{101}(t) \\ e_{011}(t) \\ e_{110}(t) \end{bmatrix} \tag{3.6}$$

The above equation suggests that $\psi_{100}(t), \psi_{010}(t)$ and $\psi_{001}(t)$ are each separated by a pulse duration of τ_p from each other. Thus,

$$\begin{aligned} \psi_{010}(t) &= \psi_{100}(t-\tau_p) \\ \psi_{001}(t) &= \psi_{100}(t-2\tau_p) \end{aligned} \tag{3.7}$$

To decode the coded OTDR traces, one should multiply the equation 3.6 by the inverse Simplex matrix S^{-1}.

$$S^{-1} = \frac{1}{2}\begin{bmatrix} 1 & -1 & 1 \\ -1 & 1 & 1 \\ 1 & 1 & -1 \end{bmatrix} \tag{3.8}$$

$$\begin{bmatrix} \tilde{\psi}_{100}(t) \\ \tilde{\psi}_{010}(t) \\ \tilde{\psi}_{001}(t) \end{bmatrix} = S^{-1} \begin{bmatrix} \psi_{101}(t) \\ \psi_{011}(t) \\ \psi_{110}(t) \end{bmatrix} \tag{3.9}$$

$$= \frac{1}{2}\begin{bmatrix} \psi_{101}(t) - \psi_{011}(t) + \psi_{110}(t) \\ -\psi_{101}(t) + \psi_{011}(t) + \psi_{110}(t) \\ \psi_{101}(t) + \psi_{011}(t) - \psi_{110}(t) \end{bmatrix}$$

$$= \begin{bmatrix} \psi_{100}(t) + \dfrac{e_{101}(t) - e_{011}(t) + e_{110}(t)}{2} \\ \psi_{010}(t) + \dfrac{-e_{101}(t) + e_{011}(t) + e_{110}(t)}{2} \\ \psi_{001}(t) + \dfrac{e_{101}(t) + e_{011}(t) - e_{110}(t)}{2} \end{bmatrix} \tag{3.10}$$

where $\tilde{\psi}_{ijk}$ denotes the estimated single pulse response of the system after decoding. The decoded traces are delayed by pulse duration τ_p from each other. Thus,

$$\begin{aligned} \tilde{\psi}_{010}(t) &= \tilde{\psi}_{100}(t-\tau_p) \\ \tilde{\psi}_{001}(t) &= \tilde{\psi}_{100}(t-2\tau_p) \end{aligned} \tag{3.11}$$

The time delay between decoded traces can be aligned in the time-domain by shifting $\tilde{\psi}_{010}(t)$, and $\tilde{\psi}_{001}(t)$ by τ_p, and $2\tau_p$ respectively. Finally, the average of aligned traces must be taken. Then, the final retrieved OTDR trace $\Psi(t)$ that corresponds to the overall single pulse response of the system is as follows;

$$\begin{aligned}\Psi(t) =& \frac{\tilde{\psi}_{100}(t) + \tilde{\psi}_{010}(t+\tau_p) + \tilde{\psi}_{001}(t+2\tau_p)}{3} \\ =&\psi_{100}(t) + \frac{1}{6}\Bigg\{ e_{101}(t) - e_{011}(t) + e_{110}(t) + \\ & - e_{101}(t+\tau_p) + e_{011}(t+\tau_p) + e_{110}(t+\tau_p) + \\ & e_{101}(t+2\tau_p) + e_{011}(t+2\tau_p) - e_{110}(t+2\tau_p)\Bigg\}\end{aligned} \tag{3.12}$$

3.3 SNR Analysis of the Simplex Coding Scheme

Recalling the assumption that the noise is AWGN with a mean value of zero and variance of σ^2, and is uncorrelated;

$$E\{e_{ijk}(t)\} = 0 \tag{3.13}$$

$$E\{e_{ijk}^2(t)\} = \sigma^2 \tag{3.14}$$

$$E\{e_{ijk}(t), e_{lmn}(t)\} = 0\ ,(ijk \neq lmn) \tag{3.15}$$

The mean squared error (MSE) of the final trace is as follows;

$$E\left\{(\Psi(t) - \psi_{100}(t))^2\right\} = \frac{9}{36}\sigma^2 = \frac{1}{4}\sigma^2 \tag{3.16}$$

Note that the finally retrieved trace is the average of 3 separate traces, as the code length $L = 3$. Thus, one should include the MSE of $N = 3$ traditional averaging as well, which is $\sigma^2/3$. Thereby, the SNR improvement is found to be as follows;

$$\sqrt{\frac{\sigma^2}{3} / \frac{\sigma^2}{4}} = \frac{2}{\sqrt{3}} \tag{3.17}$$

However, this result is valid only for $L = 3$. To get a more general expression for the SNR improvement with any code length L, below equation is derived;

$$G_{SC} = \frac{L+1}{2\sqrt{L}} \tag{3.18}$$

where, G_{SC} is called the *coding gain* for Simplex coding scheme. Figure 3.1 shows the coding gain in dB as a function of code length L.

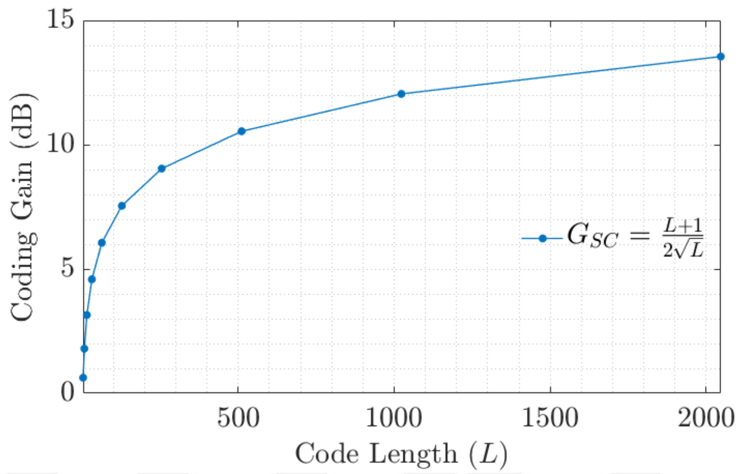

Figure 3.1: Coding gain of Simplex coding scheme.

It is proven that using Simplex codes can increase the SNR of the system under the same measurement time as traditional interrogation. The method preserves the spatial resolution of a single pulse. The only setback of this method is that the EDFA's transient effect should be taken into account. The result of this effect is unequal amplitude of the pulses within the codeword, following an exponential decaying profile. This effect is also detrimental to the Golay coding scheme. To overcome this challenge, pre-shaping and advanced techniques such as automatic gain control (AGC) [68], different decoding algorithms [69] can be utilized, or a continuous wave EDFA can be used instead of a pulsed one.

Chapter 4

Experimental Setup

Experiments were conducted using both multi-mode and single-mode fibers. However, the signal processing, as well as electronics such as the analog-to-digital converter (ADC), digital-to-analog converter (DAC), and FPGA, are the same in both cases.

At its fundamentals, an optical pulse launches into the sensing fiber, and the backscattered Raman signal is detected by APDs at the receiving end. A DAC is used to create an electronic signal for external modulation of the laser or an input RF signal for the acousto-optic modulator (AOM). The injected pulse passes through a Raman wavelength division multiplexer (WDM). The purpose of Raman WDM is twofold: to couple the backscattered Raman Stokes and anti-Stokes wavelengths into different optical paths; to filter out Rayleigh and Brillouin scattering, as they will contribute to the noise in the measurement. The Raman WDM component also has an optical circulator in it. The circulator ensures that the injected optical pulses travel into the sensing fiber while routing the backscattered Raman signals toward the detection system without interference from the input.

Finally, two APDs are employed for the simultaneous detection of Stokes and anti-Stokes wavelengths. The optical signal is then converted to an electronic signal by APDs. An ADC is utilized to digitize the APD readout. FPGA is the main building block for the experimental realization of all the concepts mentioned in the earlier chapters. It produces the desired electronic signal to create optical pulses —also the pulse coding scheme. Figure 4.1 explains the algorithm in a flow chart, including the post-processing sequences.

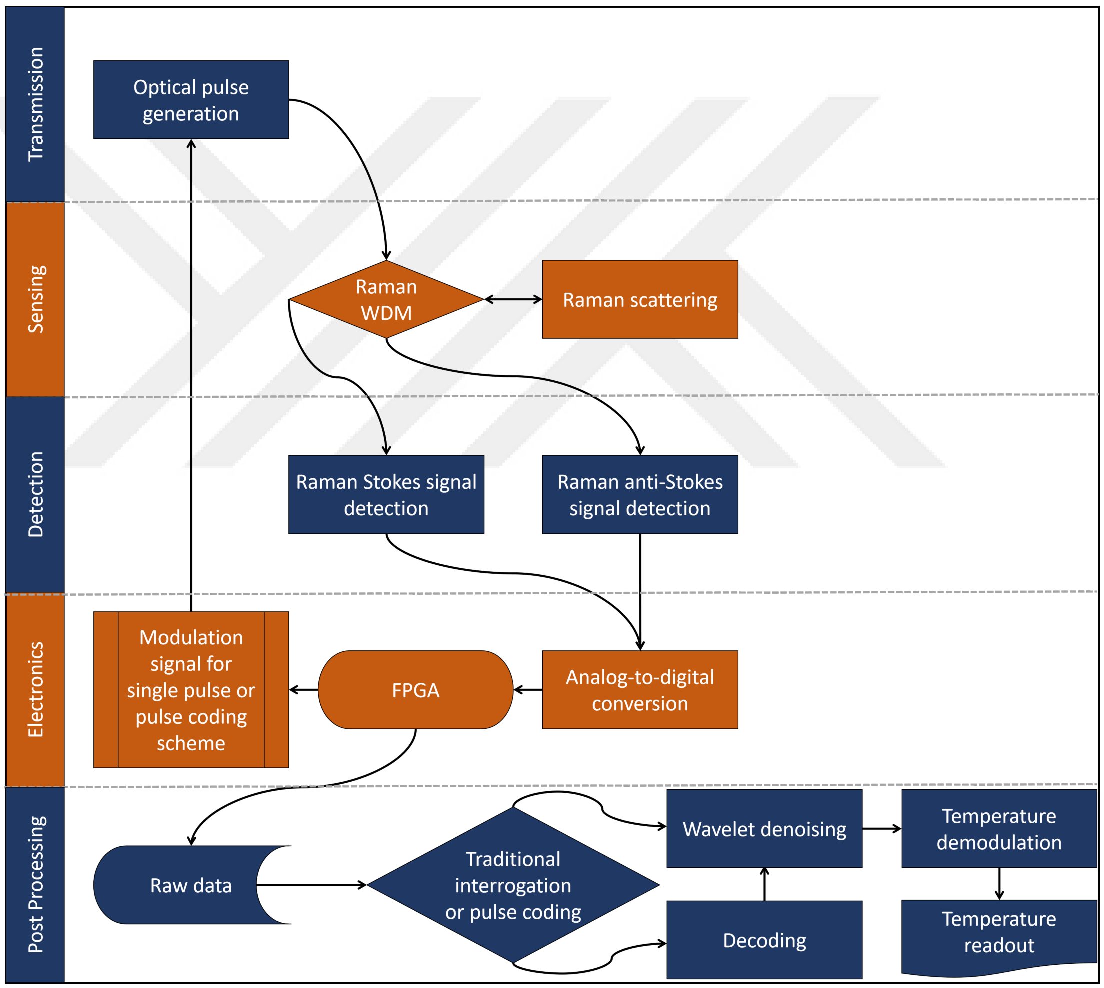

Figure 4.1: Flow chart for the experimental setup, including the post processing.

4.1 Multi-Mode Fiber Based RDTS Setup

Figure 4.2 illustrates the experimental setup for MMF. A pulsed laser is externally triggered by a trigger signal generated by the FPGA. Graded-index MMF with $50\mu m$ core and $125\mu m$ cladding radius is utilized as the sensing fiber. About $200m$ of reference coil is used for calibration. $50m$ of fiber under test (FUT) is placed in a temperature-controlled box to heat up the fiber. The backscattered Raman signal is measured by MMF pigtailed APDs, then the APD readout is converted to a digital signal by a 15-bit, $256MSa/s$ ADC for signal processing. Due to the Nyquist sampling theorem, ADC has a frequency bandwidth of $128MHz$. Notice that $128MHz$ corresponds to a period of $\approx 8ns$. Thus, ADC detects the optical power averaged over $8ns$. In other words, it detects the optical power averaged over $nu \cdot (8 \times 10^{-9}s) \approx 1.6m$ $, where \nu = 2 \times 10^{8} ms^{-1}$ is the speed of light in fiber.

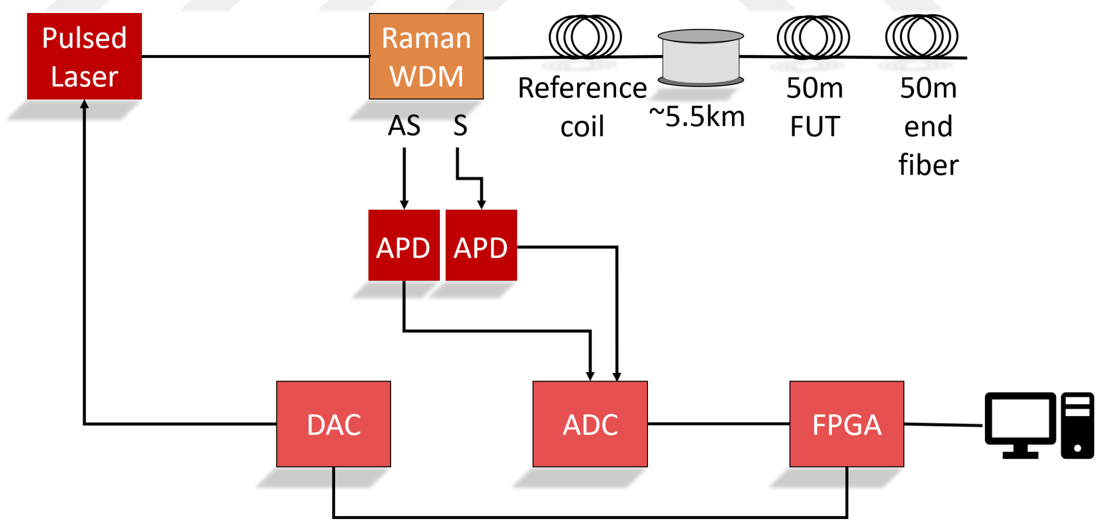

Figure 4.2: Schematics of the multi-mode fiber experimental setup.

4.2 Single-Mode Fiber Based RDTS Setup

Similarly, Figure 4.3 illustrates the experimental setup for SMF. However, there are certain differences compared to the MMF setup. Here, a continuous-wave (CW) laser is used. The output of the laser is then modulated into pulses using an acousto-optic modulator (AOM). Because the optical pulses do not have enough peak power for interrogation, a pulsed erbium-doped fiber amplifier (EDFA) is used to amplify the optical pulses. SMF-28 fiber is used as the sensing fiber with $9\mu m$ core, and $125\mu m$ cladding radius. The choice of pulsed EDFA causes a transient effect between the coded pulses. It should be noted that the transient effect within individual pulses is also there. The Frantz-Nodvik model is widely used in the literature to mitigate the transient effect caused by EDFA, but this model can fix only one optical pulse. In the case of pulse coding —where many pulses are used, this model cannot mitigate the transient effect. However, the transient effects between the coded pulses are only severe for longer bit lengths ($L \geq 31$). APDs in this setup are different than the MMF setup, as they would require an SMF pigtail. Besides the differences between the two setups, this thesis does not directly compare the experimental results of each setup. The analyses are conducted independently.

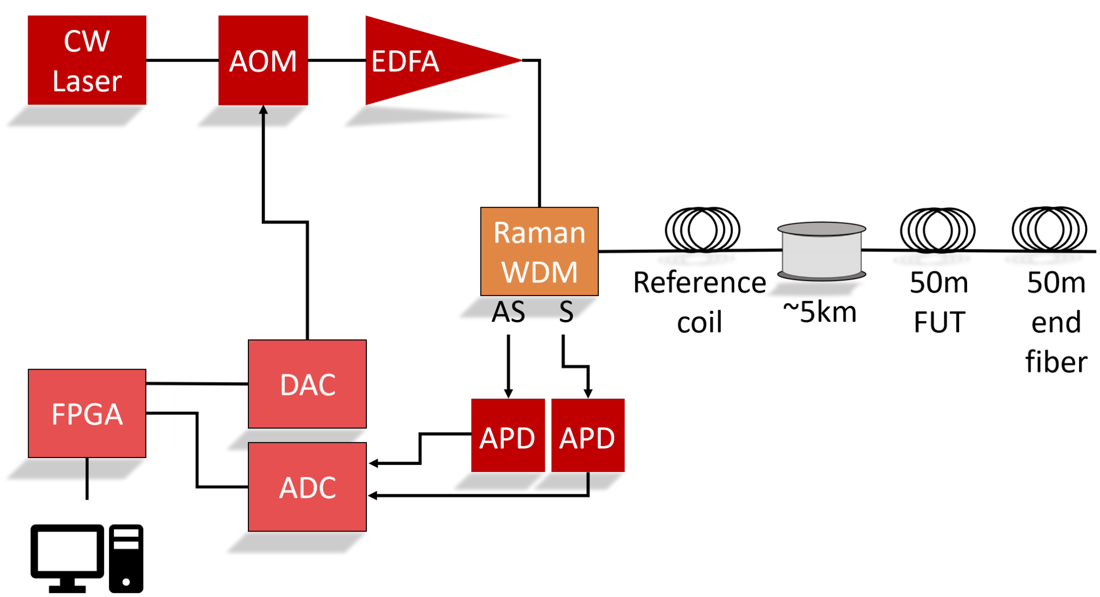

Figure 4.3: Schematics of the single-mode fiber experimental setup.

As the effective mode area A of an SMF is smaller than that of an MMF, the power threshold for the optical nonlinearity regime is also lower. For that reason, it is critical to determine the threshold. Figure 4.4 is the experimental observation of MI within the scope of this thesis. As shown in the figure, at a peak power of $P_0 \approx 25dBm$, the modulation instability appears in the optical spectrum. With increased power up to $P_0 \approx 35dBm$, SRS appears, and the probe power reduces due to pump depletion.

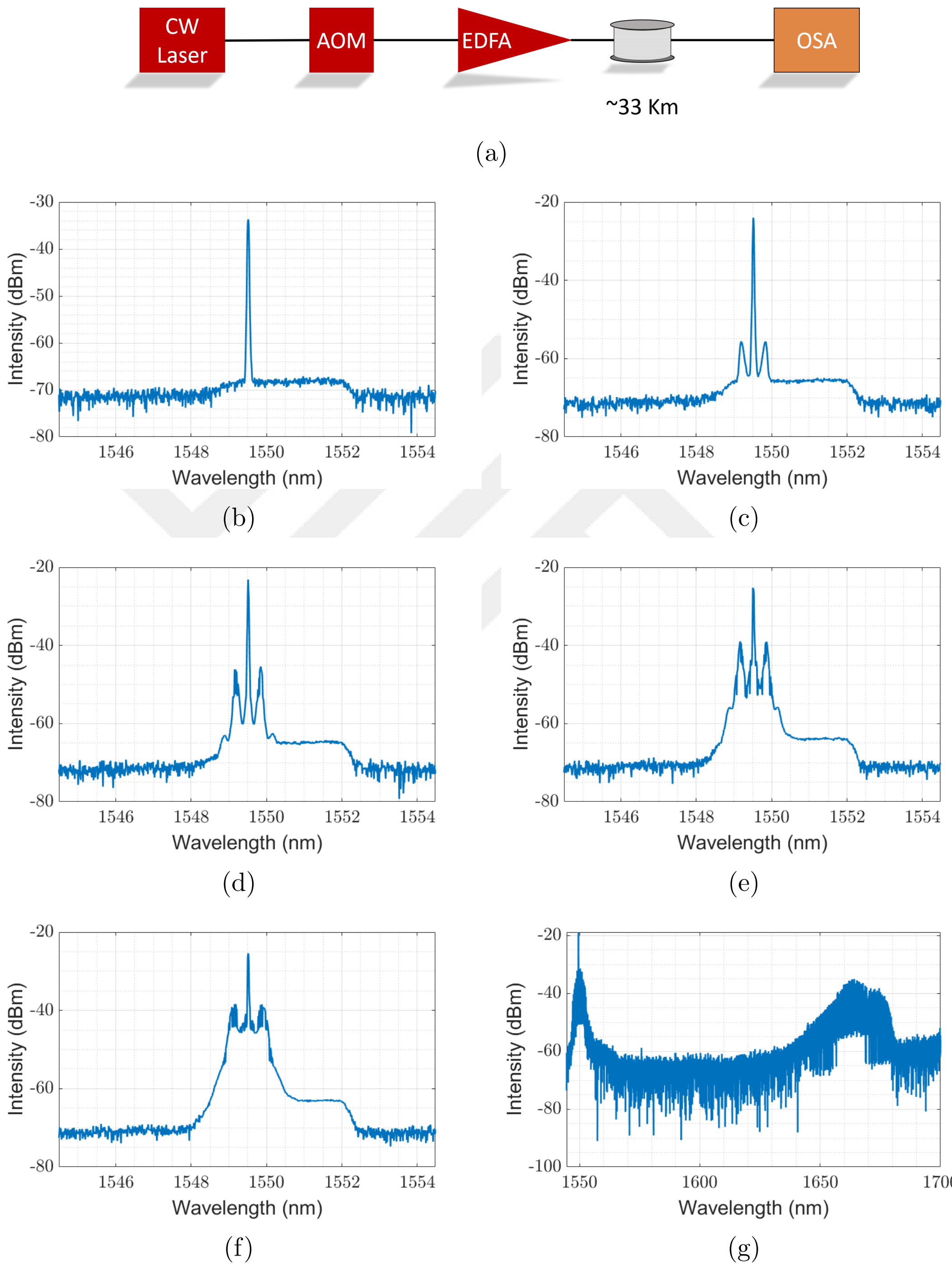

Figure 4.4: Optical spectrum after a propagation distance of $33km$ at various peak powers. (a) $P_0 = 20.77dBm$, the spectrum consists of laser and the amplified spontaneous emission (ASE) due to EDFA; (b) $P_0 = 24.84dBm$, where modulation instability is observed with symmetric sidelobes around laser wavelength; (c) $P_0 = 25.86dBm$; (d) $P_0 = 26.83dBm$; (e) $P_0 = 27.78dBm$; (f) $P_0 \approx 35dBm$, where stimulated Raman scattering (SRS) is observed.

In this chapter, the experimental setups used for MMF and SMF distributed temperature sensing are described. Key components such as the FPGA-based external modulation, Raman WDM with integrated circulator, OTDR-based detection, and FPGA-based data acquisition were outlined. Special consideration for the EDFA transient effect in the SMF setup was also discussed. The setups described here provide the experimental basis for the performance evaluation and data analysis presented in the following chapter.

Chapter 5

Analyses and Results

In this chapter, experimental results are presented for both MMF and SMF setups. MMF experiments are conducted using the traditional interrogation method —single pulse interrogation. Whereas, SMF experiments are highlighting the Simplex coding technique. The purpose of MMF experiments is to demonstrate RDTS technology, as well as the Wavelet denoising method.

5.1 Temperature Demodulation and Wavelet Denoising

Figure 5.1 highlights the improvement in temperature demodulation due to the Wavelet denoised Raman signal. There is an FUT located at around $5.5km$, and is heated to $30C^{\circ}$. Whereas, the remaining part of the sensing fiber is at room temperature $20C^{\circ}$. Due to the length of the fiber, the repetition rate is $f_{rep} \approx 16kHz$. Each second of measurement corresponds to 16,000 OTDR frames. Table 5.1 summarizes the experimental parameters used in the experiment. The blue curve depicts the temperature demodulation using the raw data —averaged over 2 seconds. Whereas, the orange curve represents the temperature demodulation using the Wavelet denoised Raman signal (also averaged over 2 seconds). It is evident that Wavelet denoising has greatly reduced the high-frequency oscillations in the raw data. The improvement is more pronounced in the temperature resolution. From the Figure 5.2, it is observed that temperature resolution at $z = 5.5km$ is improved from $\sim 0.45C^{\circ}$ to $\sim 0.10C^{\circ}$ due to Wavelet denoising.

Interrogation period (τ_i)	$60\mu s$
Repetition rate (f_{rep})	$16kHz$
Pulse duration (τ_p)	$50ns$
Peak power (P_0)	$10W$
Sampling rate	$256MSa/s$
Time averaging	$2s$
FUT temperature (T_{FUT})	$30 - 80C^{\circ}$

Table 5.1: Experimental parameters for MMF setup.

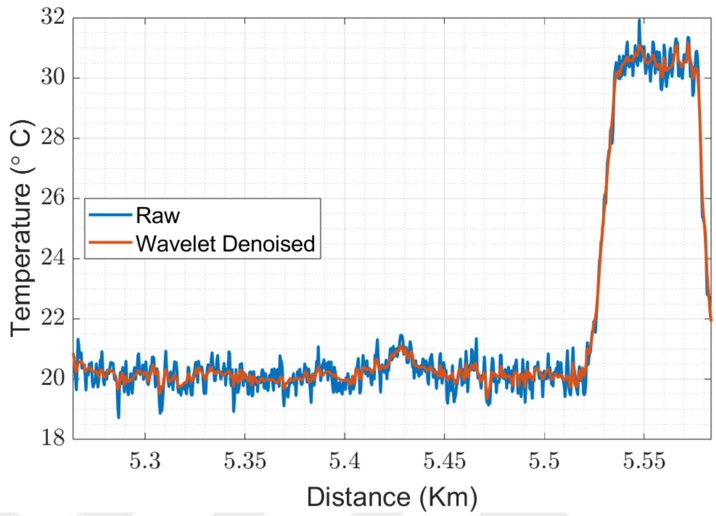

Figure 5.1: Demonstration of Wavelet denoising.

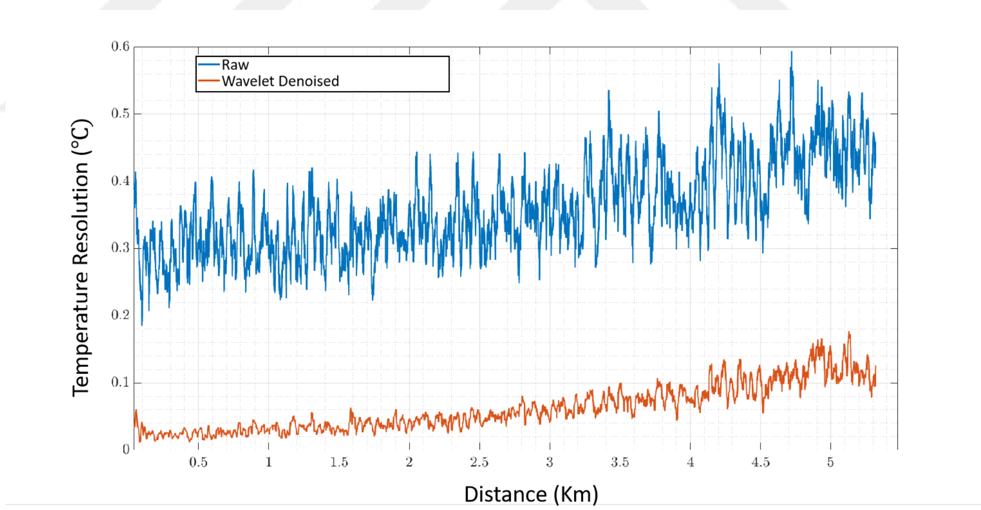

Figure 5.2: Comparing the temperature resolution of raw and Wavelet denoised signal.

Figure 5.3 demonstrates the temperature demodulation near the FUT region at different temperature values. The FUT is located at around $5.5km$, and is heated up from $40C^{\circ}$ to $80C^{\circ}$. Whereas, the remaining part of the sensing fiber is at room temperature $18C^{\circ}$. The experimental parameters are the same as table 5.1. Peak power of $10W$ is just below the SRS threshold for the MMF used in the experiment. The system is able to demodulate temperature within $\pm 1C^{\circ}$ accuracy for $2s$ of averaging.

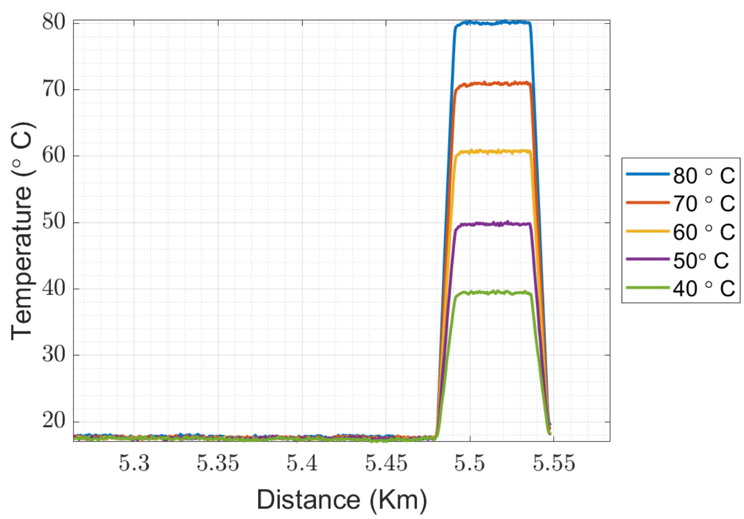

Figure 5.3: Demonstration of temperature demodulation near FUT region.

Spatial resolution of the system is also analyzed. A widely adopted definition of spatial resolution in the literature is the distance between 10% and 90% of a rising edge in the temperature curve. In the Figure 5.4, FUT is heated up to $50C^{\circ}$, while the remaining sensing fiber is at room temperature $20C^{\circ}$. The temperature difference between the FUT and the remaining fiber is $\Delta T = 30C^{\circ}$. 10% and 90% rise of the temperature corresponds to the location where the temperature is $23C^{\circ}$ and $47C^{\circ}$ respectively. These locations are marked with vertical bars in the figure and pointed with arrows. Spatial resolution is the distance between these points, which is found to be $2.8m$ at $z \approx 5.5km$. However, the pulse duration is narrowed down to $20ns$ to increase spatial resolution. Better spatial resolution can be achieved with narrower pulses, but a high-speed APD will be needed to detect backscattered Raman signals from such a shorter pulse.

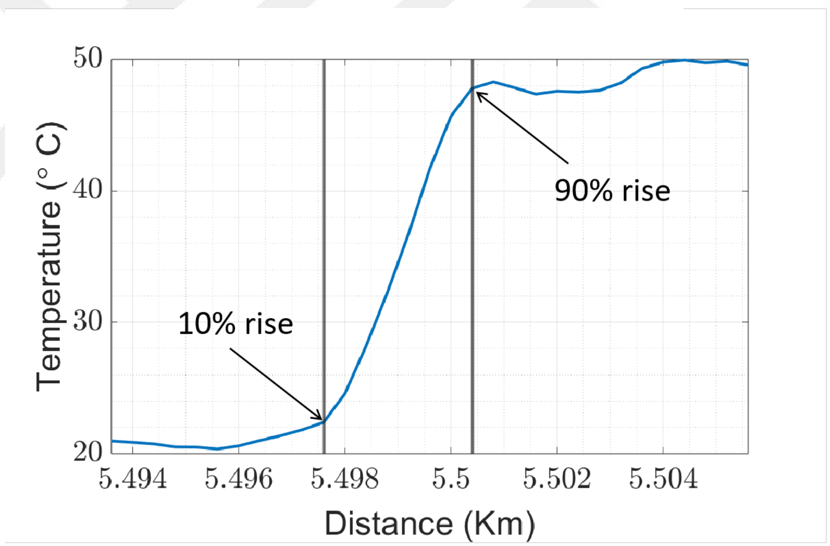

Figure 5.4: Spatial resolution of the MMF RDTS setup.

5.2 7-bit Simplex Coding

An RDTS system using SMF as the sensing fiber has lower SNR than that of MMF. This is because the nonlinear optical power threshold is significantly lower in SMFs compared to MMFs. In fact, modulation instability is observed in SMF at $P_0 = 400mW$, whereas SRS is observed at $P_0 \approx 600mW$. Interrogating the fiber with $P_0 < 400mW$ results in a reduced SNR. Pulse coding plays an important role here to increase SNR. In the following experiments, a 7-bit long Simplex coding scheme is presented. Experimental parameters are presented in the table below. Figure 5.5 below is the oscilloscope measurement of optical pulses corresponding to each codeword used for interrogation.

Interrogation period (τ_i)	$60\mu s$
Repetition rate (f_{rep})	$16kHz$
Pulse duration (τ_p)	$100ns$
Peak power (P_0)	$300mW$
Sampling rate	$256MSa/s$
Time averaging	$2s$
FUT temperature (T_{FUT})	$40C^{\circ}$

Table 5.2: Experimental parameters for SMF setup.

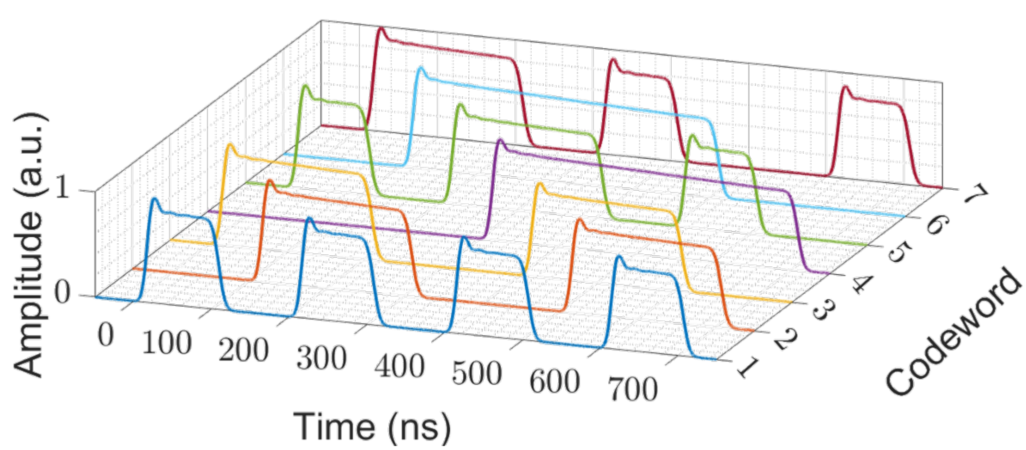

Figure 5.5: Oscilloscope measurement of optical pulses corresponding to 7-bit Simplex codewords.

The corresponding Simplex matrix is as follows:

$$S = \begin{bmatrix} 1 & 0 & 1 & 0 & 1 & 0 & 1 \\ 0 & 1 & 1 & 0 & 0 & 1 & 1 \\ 1 & 1 & 0 & 0 & 1 & 1 & 0 \\ 0 & 0 & 0 & 1 & 1 & 1 & 1 \\ 1 & 0 & 1 & 1 & 0 & 1 & 0 \\ 0 & 1 & 1 & 1 & 1 & 0 & 0 \\ 1 & 1 & 0 & 1 & 0 & 0 & 1 \end{bmatrix} = \begin{bmatrix} S_1 \\ S_2 \\ S_3 \\ S_4 \\ S_5 \\ S_6 \\ S_7 \end{bmatrix} \tag{5.1}$$

The OTDR traces are decoded by the following inverse Simplex matrix:

$$S^{-1} = \frac{1}{2} \begin{bmatrix} 1 & -1 & 1 & -1 & 1 & -1 & 1 \\ -1 & 1 & 1 & -1 & -1 & 1 & 1 \\ 1 & 1 & -1 & -1 & 1 & 1 & -1 \\ -1 & -1 & -1 & 1 & 1 & 1 & 1 \\ 1 & -1 & 1 & 1 & -1 & 1 & -1 \\ -1 & 1 & 1 & 1 & 1 & -1 & -1 \\ 1 & 1 & -1 & 1 & -1 & -1 & 1 \end{bmatrix} \tag{5.2}$$

Figure 5.6a shows the Raman anti-Stokes OTDR traces near FUT after the decoding process. The decoded traces are in agreement with theory, each trace is separated by a pulse duration of $\tau_p = 100ns$. Recall that decoded traces represent the single pulse response of the system. However, they need to be aligned in the time domain. Figure 5.6b shows the aligned Raman anti-Stokes traces near FUT. After the alignment process, an average of 7 traces is taken. The same procedure is also performed for the Raman Stokes component. Then, Wavelet denoising and temperature demodulation are performed for the recently obtained Raman signals.

Figure 5.7a compares the demodulated temperature of traditional interrogation —single pulse —and 7-bit Simplex coded interrogation. From the graph, it is clear that signal noise is suppressed, and the oscillations in the signal are much less compared to traditional interrogation. The performance improvement is more pronounced in the temperature resolution graph shown in Figure 5.7b. Due to exponential attenuation of the optical pulses —Beer-Lambert attenuation —temperature resolution accordingly deteriorates with distance. The exponential deterioration of temperature resolution is observed in the measurements. On the other hand, it is hard to see this exponential deterioration in the temperature resolution graph presented in Figure 5.2 simply because the optical power is much higher in MMF experiments. It is also noticeable that the temperature resolution of the SMF setup is worse than the MMF setup, due to a much lower nonlinear optical power threshold. However, it is presented that 7-bit Simplex coded interrogation improves the temperature resolution by $0.5C^{\circ}$ at $z = 5km$.

In this chapter, the experimental results for both MMF and SMF are presented. The results show the effectiveness of Wavelet denoising and Simplex coding to improve temperature demodulation performance of the RDTS system. While the Wavelet denoising method does not increase the system complexity, the Simplex coding method slightly increases the complexity of the system design.

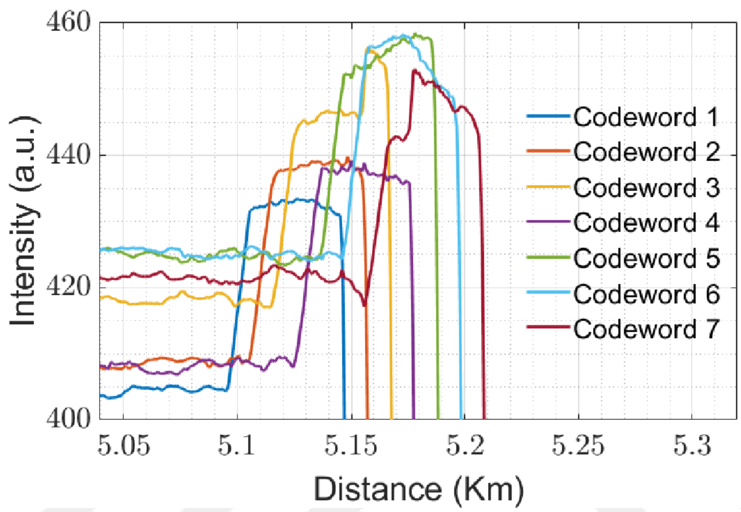

(a)

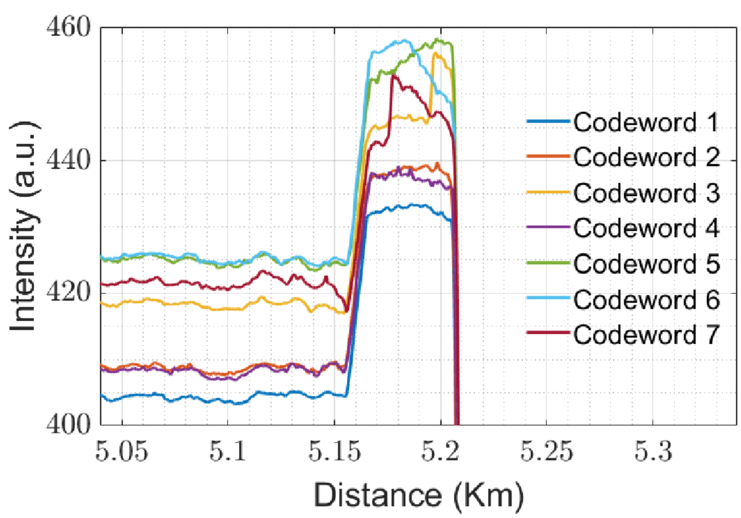

(b)

Figure 5.6: (a) decoded Raman anti-Stokes OTDR traces; (b) decoded and aligned Raman anti-Stokes OTDR traces in time-domain.

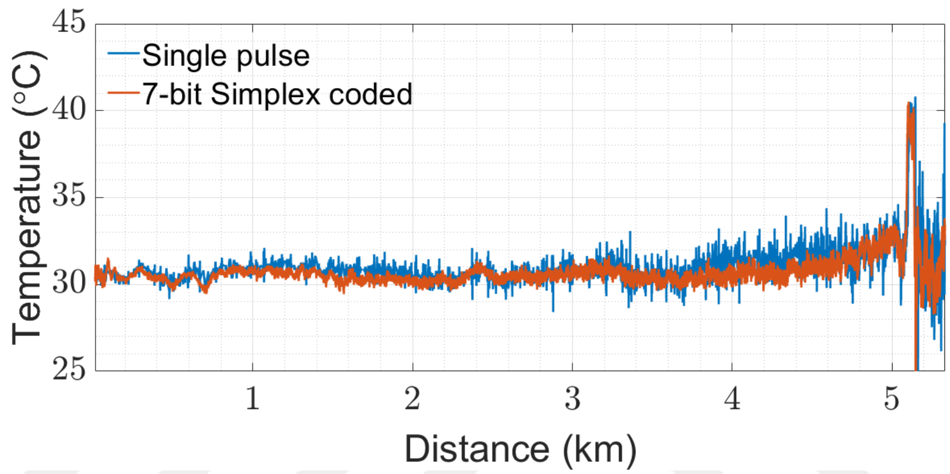

(a)

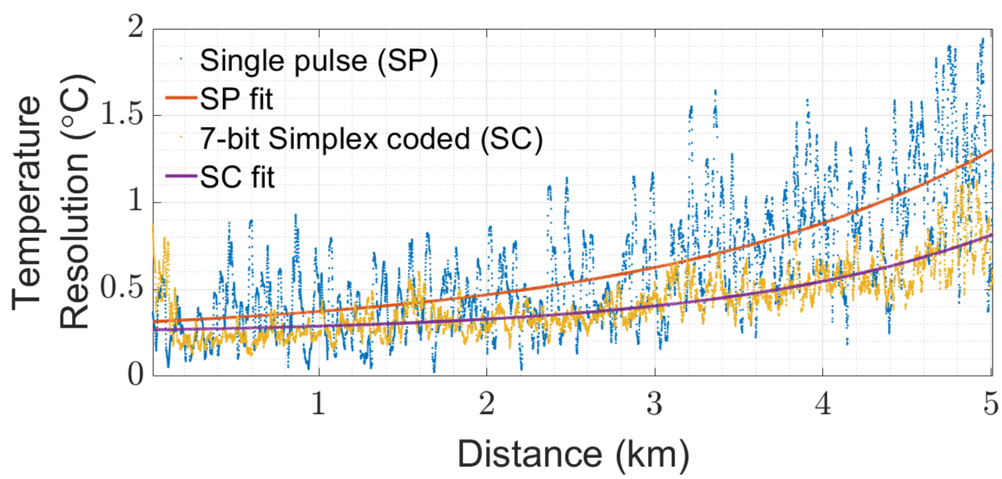

(b)

Figure 5.7: (a) temperature demodulation of traditional interrogation vs 7-bit Simplex coded interrogation; (b) temperature resolution of traditional interrogation vs 7-bit Simplex coded interrogation.

Chapter 6

Conclusion and Future Work

RDTS technology is an excellent solution for monitoring the temperature of inaccessible or large areas. It is a widely used technology in fire detection and structural health monitoring of tunnels, railways, pipelines, and more. However, due to the inherently weak nature of Raman scattering, temperature demodulation at longer distances becomes difficult to achieve.

In this thesis, RDTS technology is studied. Chapter 2 reviewed concepts from optical pulse propagation inside the optical fiber to the noise sources of the system. The details of Raman scattering are also discussed in Chapter 2. The discussion is then followed by an explanation of the DTS technology in detail. Later, the Simplex coding method is discussed with mathematical constructions.

After building the intuition and the theoretical background, the experimental setup is presented in Chapter 5. The experimental details of DTS technology are explained through system schematics. The effectiveness of Wavelet denoising is demonstrated through experiments. After implementing Wavelet denoising, the temperature resolution is improved from $0.45C^{\circ}$ to $0.10C^{\circ}$ at $z = 5.5km$. Determination of spatial resolution is also demonstrated in the MMF experiments. Using a pulse duration of $\tau_p = 20ns$, the system had $2.8m$ spatial resolution at $z = 5.5km$.

As for SMF experiments, since 7-bit long Simplex coding is presented in the thesis, a pulsed EDFA is used without hesitation. However, implementing advanced techniques such as automatic gain control, pre-shaping, or using a CW EDFA is definitely required for longer bits to mitigate the transient effect between the coded pulses. The results showed an improvement in temperature resolution from $1.3°C$ to $0.8°C$ at $z = 5km$.

It is shown that implementing Wavelet denoising does not increase the system complexity. On the other hand, including Simplex coding in the system slightly increases the complexity due to the EDFA transient effect. However, given that Raman scattering is so weak in optical power, the advantage of Simplex coding is worth the added system complexity, especially in achieving long-distance temperature sensing. Longer bit lengths can be used to further increase the system performance of a Simplex coded RDTS system —a special consideration of the EDFA transient effect is needed.

For future work, novel coding schemes can be studied to simultaneously improve spatial resolution and sensing distance. Chaotic complex systems can generate pseudo-random and orthogonal binary codes [70]. The literature shows that a radar's ambiguity function is improved by a coding scheme generated using the Bernoulli map [71]. The advantages of using such a coding scheme can be transferred to RDTS technology.

Bibliography

[1] S. Singh and R. Kaler, "Placement of optimized semiconductor optical amplifier in fiber optical communication systems," *Optik*, vol. 119, no. 6, pp. 296–302, 2008.

[2] H. K. Soong and J. B. Malta, "Femtosecond lasers in ophthalmology," *American Journal of Ophthalmology*, vol. 147, no. 2, pp. 189–197.e2, 2009.

[3] H. He, L. Jiang, Y. Pan, A. Yi, X. Zou, W. Pan, A. E. Willner, X. Fan, Z. He, and L. Yan, "Integrated sensing and communication in an optical fibre," *Light: Science & Applications*, vol. 12, p. 25, 01 2023.

[4] Y. N. Korkishko, V. Fedorov, V. Prilutskii, V. Ponomarev, V. Marchuk, I. Morev, S. Kostritskii, E. Paderin, L. Nesenyuk, A. Buravlev, *et al.*, "Navigation-grade interferometric fiber optical gyroscope," in *14th St. Petersburg International Conference on Integrated Navigation Systems*, pp. 138–143, Elektropribor St. Petersburg, 2007.

[5] D. Stellinga, D. B. Phillips, S. P. Mekhail, A. Selyem, S. Turtaev, T. Čižmár, and M. J. Padgett, "Time-of-flight 3d imaging through multimode optical fibers," *Science*, vol. 374, no. 6573, pp. 1395–1399, 2021.

[6] E. Kakkava, B. Rahmani, N. Borhani, U. Teğin, D. Loterie, G. Konstantinou, C. Moser, and D. Psaltis, "Imaging through multimode fibers using deep learning: The effects of intensity versus holographic recording of the speckle pattern," *Optical Fiber Technology*, vol. 52, p. 101985, 2019.

[7] X. Sui, Q. Wu, J. Liu, Q. Chen, and G. Gu, "A review of optical neural networks," *IEEE Access*, vol. 8, pp. 70773–70783, 2020.

[8] S. Gigan, O. Katz, H. B. de Aguiar, E. R. Andresen, A. Aubry, J. Bertolotti, E. Bossy, D. Bouchet, J. Brake, S. Brasselet, Y. Bromberg, H. Cao, T. Chaigne, Z. Cheng, W. Choi, T. Čižmár, M. Cui, V. R. Curtis, H. Defienne, M. Hofer, R. Horisaki, R. Horstmeyer, N. Ji, A. K. LaViolette, J. Mertz, C. Moser, A. P. Mosk, N. C. Pégard, R. Piestun, S. Popoff, D. B. Phillips, D. Psaltis, B. Rahmani, H. Rigneault, S. Rotter, L. Tian, I. M. Vellekoop, L. Waller, L. Wang, T. Weber, S. Xiao, C. Xu, A. Yamilov, C. Yang, and H. Yılmaz, "Roadmap on wavefront shaping and deep imaging in complex media," *Journal of Physics: Photonics*, vol. 4, p. 042501, aug 2022.

[9] A. Demircan and U. Bandelow, "Supercontinuum generation by the modulation instability," *Optics Communications*, vol. 244, no. 1, pp. 181–185, 2005.

[10] A. N. Hartog, *An Introduction to Distributed Optical Fibre Sensors*. Boca Raton: CRC Press, 2017.

[11] C. Pandian, M. Kasinathan, S. Sosamma, C. Babu Rao, T. Jayakumar, N. Murali, V. Paunikar, S. Kumar, K. Rajan, and B. Raj, "Raman distributed sensor system for temperature monitoring and leak detection in sodium circuits of fbr," in *2009 1st International Conference on Advancements in Nuclear Instrumentation, Measurement Methods and their Applications*, pp. 1–4, 2009.

[12] B. Yan, J. Li, M. Zhang, J. Zhang, L. Qiao, and T. Wang, "Raman distributed temperature sensor with optical dynamic difference compensation and visual localization technology for tunnel fire detection," *Sensors*, vol. 19, no. 10, 2019.

[13] I. Ashry, Y. Mao, B. Wang, F. Hveding, A. Y. Bukhamsin, T. K. Ng, and B. S. Ooi, "A review of distributed fiber–optic sensing in the oil and gas industry," *J. Lightwave Technol.*, vol. 40, pp. 1407–1431, Mar 2022.

[14] P. Velha, T. Nannipieri, A. Signorini, M. Morosi, M. Solazzi, F. Barone, A. Frisoli, L. Ricciardi, S. Giuliani, R. Eusepi, M. Icardi, G. Recchia,

M. Lupi, G. Arcoleo, P. Firmi, and F. Di Pasquale, “Monitoring large railways infrastructures using hybrid fbg/raman sensor systems,” in *20th Italian National Conference on Photonic Technologies (Fotonica 2018)*, pp. 1–3, 2018.

[15] A. Ukil, H. Braendle, and P. Krippner, “Distributed temperature sensing: Review of technology and applications,” *IEEE Sensors Journal*, vol. 12, no. 5, pp. 885–892, 2012.

[16] J. Dakin, D. Pratt, G. Bibby, and J. Ross, “Distributed antistokes ratio thermometry,” in *Optical Fiber Sensors*, p. PDS3, Optica Publishing Group, 1985.

[17] J. Dakin, D. Pratt, G. Bibby, and J. Ross, “Distributed optical fibre raman temperature sensor using a semiconductor light source and detector,” *Electronics Letters*, vol. 21, pp. 569–570, 1985.

[18] Z. Zhang, H. Wu, C. Zhao, and M. Tang, “High-performance raman distributed temperature sensing powered by deep learning,” *Journal of Lightwave Technology*, vol. 39, no. 2, pp. 654–659, 2021.

[19] J. Li and M. Zhang, “Physics and applications of raman distributed optical fiber sensing,” *Light: Science Applications*, vol. 11, p. 128, 2022.

[20] N. Van de Giesen, S. C. Steele-Dunne, J. Jansen, O. Hoes, M. B. Hausner, S. Tyler, and J. Selker, “Double-ended calibration of fiber-optic raman spectra distributed temperature sensing data,” *Sensors*, vol. 12, no. 5, pp. 5471–5485, 2012.

[21] M. A. Soto and L. Thévenaz, “Advanced pulse coding techniques for distributed optical fiber sensors,” in *Frontiers in Optics 2013*, p. FW4I.3, Optica Publishing Group, 2013.

[22] J. Li, X. Zhou, Y. Xu, L. Qiao, J. Zhang, and M. Zhang, “Slope-assisted raman distributed optical fiber sensing,” *Photon. Res.*, vol. 10, pp. 205–213, Jan 2022.

[23] J. Li, C. Wang, K. Cao, B. Fan, X. Zhou, Y. Xu, Z. Cheng, Q. Zhang, L. Qiao, X. Xue, J. Zhang, and M. Zhang, "Breakthrough the physical barrier on spatial resolution in raman distributed fiber sensing using chaotic correlation demodulation," *APL Photonics*, vol. 8, p. 076105, 07 2023.

[24] P. Li, Y. Wang, P. Wang, Q. Bai, Y. Gao, H. Zhang, and B. Jin, "Pulse coding in distributed optical fiber vibration sensor: A review," *IEEE Sensors Journal*, vol. 21, no. 20, pp. 22371–22387, 2021.

[25] X. Sun, Z. Yang, X. Hong, S. Zaslawski, S. Wang, M. A. Soto, X. Gao, J. Wu, and L. Thévenaz, "Genetic-optimised aperiodic code for distributed optical fibre sensors," *Nature Communications*, vol. 11, no. 1, p. 5774, 2020.

[26] D. Lee, H. Yoon, N. Y. Kim, H. Lee, and N. Park, "Analysis and experimental demonstration of simplex coding technique for snr enhancement of otdr," in *Proceedings of the Lightwave Technologies in Instrumentation and Measurement Conference, 2004.*, pp. 118–122, 2004.

[27] R. Goldman, A. Agmon, and M. Nazarathy, "Direct detection and coherent optical time-domain reflectometry with golay complementary codes," *Journal of Lightwave Technology*, vol. 31, no. 13, pp. 2207–2222, 2013.

[28] H. Haderer, R. Feger, and A. Stelzer, "A comparison of phase-coded cw radar modulation schemes for integrated radar sensors," in *2014 44th European Microwave Conference*, pp. 1896–1899, 2014.

[29] J. M and M. Jamro, *Optical Fiber Communications: Principles and Practice*. Prentice Hall Internacional series in optoelectronics, Financial Times/Prentice Hall, 2009.

[30] F. Farahi and J. L. Santos, eds., *Handbook of Optical Sensors*. CRC Press, 2014.

[31] G. Agrawal, *Nonlinear Fiber Optics*. Optics and Photonics, Boston: Academic Press, fifth edition ed., 2013.

[32] C. Fowler, S. Silva, G. Thapa, and J. Zhou, "High efficiency ambient rf energy harvesting by a metamaterial perfect absorber," *Opt. Mater. Express*, vol. 12, pp. 1242–1250, Mar 2022.

[33] D. A. Long, *Survey of Light-scattering Phenomena*, ch. 1, pp. 3–18. John Wiley Sons, Ltd, 2002.

[34] M. A. Soto, A. Signorini, T. Nannipieri, S. Faralli, and G. Bolognini, "High-performance raman-based distributed fiber-optic sensing under a loop scheme using anti-stokes light only," *IEEE Photonics Technology Letters*, vol. 23, no. 9, pp. 534–536, 2011.

[35] D. Hwang, D.-J. Yoon, I.-B. Kwon, D.-C. Seo, and Y. Chung, "Novel auto-correction method in a fiber-optic distributed-temperature sensor using reflected anti-stokes raman scattering," *Opt. Express*, vol. 18, pp. 9747–9754, May 2010.

[36] W. Ciciora, J. Farmer, D. Large, and M. Adams, "Chapter 19 - digital fiber modulation and deep fiber architectures," in *Modern Cable Television Technology (Second Edition)* (W. Ciciora, J. Farmer, D. Large, and M. Adams, eds.), The Morgan Kaufmann Series in Networking, pp. 767–787, San Francisco: Morgan Kaufmann, second edition ed., 2004.

[37] B. Carter, "Chapter 12 - op amp noise theory and applications," in *Op Amps for Everyone (Third Edition)* (R. Mancini and B. Carter, eds.), pp. 163–188, Boston: Newnes, third edition ed., 2009.

[38] T. Blain, V. Shulyak, I. S. Han, M. Hopkinson, J. S. Ng, and C. H. Tan, "Low noise equivalent power inas avalanche photodiodes for infrared few-photon detection," *IEEE Transactions on Electron Devices*, vol. 71, no. 5, pp. 3039–3044, 2024.

[39] B. Sun, J. Chang, J. Lian, Z. Wang, G. Lv, X. Liu, W. Wang, S. Zhou, W. Wei, S. Jiang, Y. Liu, S. Luo, X. Liu, Z. Liu, and S. Zhang, "Accuracy improvement of raman distributed temperature sensors based on eliminating rayleigh noise impact," *Optics Communications*, vol. 306, pp. 117–120, 2013.

[40] R. Acharya, "Chapter 5 - navigation receiver," in *Understanding Satellite Navigation* (R. Acharya, ed.), pp. 155–215, Oxford: Academic Press, 2014.

[41] J. Li, B. Yan, M. Zhang, J. Zhang, B. Jin, Y. Wang, and D. Wang, "Long-range raman distributed fiber temperature sensor with early warning model for fire detection and prevention," *IEEE Sensors Journal*, vol. 19, no. 10, pp. 3711–3717, 2019.

[42] M. K. Saxena, S. Raju, R. Arya, R. Pachori, S. Ravindranath, S. Kher, and S. Oak, "Raman optical fiber distributed temperature sensor using wavelet transform based simplified signal processing of raman backscattered signals," *Optics Laser Technology*, vol. 65, pp. 14–24, 2015.

[43] J. J. Lee, S. M. Lee, I. Y. Kim, H. K. Min, and S. H. Hong, "Comparison between short time fourier and wavelet transform for feature extraction of heart sound," in *Proceedings of IEEE. IEEE Region 10 Conference. TENCON 99. 'Multimedia Technology for Asia-Pacific Information Infrastructure' (Cat. No.99CH37030)*, vol. 2, pp. 1547–1550 vol.2, 1999.

[44] M. K. Saxena, S. Raju, R. Arya, S. Ravindranath, S. Kher, and S. Oak, "Optical fiber distributed temperature sensor using short term fourier transform based simplified signal processing of raman signals," *Measurement*, vol. 47, pp. 345–355, 2014.

[45] W. Astuti, W. Sediono, A. Aibinu, R. Akmeliawati, and M. J. E. Salami, "Adaptive short time fourier transform (stft) analysis of seismic electric signal (ses): A comparison of hamming and rectangular window," in *2012 IEEE Symposium on Industrial Electronics and Applications*, pp. 372–377, 2012.

[46] A. A. Ahmad and A. Z. bin Sha'ameri, "Analysis and classification of airborne radar signal types using time-frequency analysis," in *2014 International Conference on Computer and Communication Engineering*, pp. 76–79, 2014.

[47] A. L. Chakraborty, S. Kher, S. Chaubey, and T. Nathan, "Bidirectional frequency-domain digital filtering to simultaneously improve temperature

resolution and eliminate spatial inaccuracy of a distributed temperature sensor," *Optical Engineering*, vol. 43, no. 11, p. 2724 – 2729, 2004. Cited by: 3.

[48] A. Jansen, "Modal identification of lightweight pedestrian bridges based on time-frequency analysis," 03 2016.

[49] G. B. Gharehpetian and H. Karami, "Chapter 5 - analyzing emws using wavelet transform," in *Power Transformer Online Monitoring Using Electromagnetic Waves* (G. B. Gharehpetian and H. Karami, eds.), pp. 89–113, Academic Press, 2023.

[50] S. G. Mallat, "Multiresolution approximations and wavelet orthonormal bases of ^{2} ()," *Transactions of the American mathematical society*, vol. 315, no. 1, pp. 69–87, 1989.

[51] S. Fouladi, A. Safaei, N. Mammone, F. Gh, and M. J. Ebadi, "Efficient deep neural networks for classification of alzheimer's disease and mild cognitive impairment from scalp eeg recordings," *Cognitive Computation*, vol. 14, 07 2022.

[52] V. Giurgiutiu, "Chapter 14 - signal processing and pattern recognition for structural health monitoring with pwas transducers," in *Structural Health Monitoring with Piezoelectric Wafer Active Sensors (Second Edition)* (V. Giurgiutiu, ed.), pp. 807–862, Oxford: Academic Press, second edition ed., 2014.

[53] W.-R. Yang, C.-S. Wang, and C.-P. Chen, "Motion-pattern recognition system using a wavelet-neural network," *IEEE Transactions on Consumer Electronics*, vol. 65, no. 2, pp. 170–178, 2019.

[54] S. Gunanandhini, M. Kalamani, M. Bhagavathipriya, and S. prasath, "Wavelet based video compression techniques for industrial monitoring applications," *Journal of Physics: Conference Series*, vol. 2272, p. 012019, 07 2022.

[55] F. Zhang, S. qian Liu, D. bao Wang, and W. Guan, "Aircraft recognition in infrared image using wavelet moment invariants," *Image and Vision Computing*, vol. 27, no. 4, pp. 313–318, 2009.

[56] H. Kwon, Y. Choi, H. Park, K. C. Oh, H. Cho, I. Moon, and J. Kim, "Distillation column temperature prediction based on machine-learning model using wavelet transform," in *14th International Symposium on Process Systems Engineering* (Y. Yamashita and M. Kano, eds.), vol. 49 of *Computer Aided Chemical Engineering*, pp. 1651–1656, Elsevier, 2022.

[57] I. A. Ershov, O. V. Stukach, I. V. Sychev, and I. B. Tsydenzhapov, "The wavelet filtration denoising in the raman distributed temperature sensing," in *2020 Dynamics of Systems, Mechanisms and Machines (Dynamics)*, pp. 1–3, 2020.

[58] M. Dávideková, M. Greguš ml., P. Farkaš, and M. Rákus, "Applications of complete complementary codes and propositions for future research areas of these codes," *Procedia Computer Science*, vol. 83, pp. 592–599, 2016. The 7th International Conference on Ambient Systems, Networks and Technologies (ANT 2016) / The 6th International Conference on Sustainable Energy Information Technology (SEIT-2016) / Affiliated Workshops.

[59] H. Xu, D. Sun, Y. Wu, X. Wang, and J. Li, "Detection range/spatial resolution enhancement of coherent doppler wind lidar based on improved simplex coding," *IEEE Transactions on Geoscience and Remote Sensing*, vol. 61, pp. 1–11, 2023.

[60] L. Qi, Y. Yao, B. Huang, and G. Wu, "A phase-coded ofdm signal for radar-communication integration," in *2019 IEEE International Symposium on Phased Array System Technology (PAST)*, pp. 1–4, 2019.

[61] Z. Fan, J. Rudlin, G. Asfis, and H. Meng, "Convolution of barker and golay codes for low voltage ultrasonic testing," *Technologies*, vol. 7, no. 4, 2019.

[62] R. Mayazumi and T. Kojima, “A blind digital steganography scheme based on complete complementary codes,” in *2011 Seventh International Conference on Intelligent Information Hiding and Multimedia Signal Processing*, pp. 45–48, 2011.

[63] G.-C. Yang, “Variable-weight optical orthogonal codes for cdma networks with multiple performance requirements,” *IEEE Transactions on Communications*, vol. 44, no. 1, pp. 47–55, 1996.

[64] M. Jones, “Using simplex codes to improve otdr sensitivity,” *IEEE Photonics Technology Letters*, vol. 5, no. 7, pp. 822–824, 1993.

[65] G. Bolognini, J. Park, P. Kim, D. Lee, F. D. Pasquale, and N. Park, “Performance enhancement of raman-based distributed temperature sensors using simplex codes,” in *Optical Fiber Communication Conference and Exposition and The National Fiber Optic Engineers Conference*, p. OTuL1, Optica Publishing Group, 2006.

[66] M. Harwit and N. J. Sloane, *Hadamard Transform Optics*. Academic Press, 1979.

[67] M. Akhavan-Bahabdi and M. Shiva, “Double orthogonal codes for increasing capacity in mc-cdma systems,” in *Second IFIP International Conference on Wireless and Optical Communications Networks, 2005. WOCN 2005.*, pp. 468–471, 2005.

[68] J. B. Rosolem, F. R. Bassan, D. E. de Freitas, and F. C. Salgado, “Raman dts based on otdr improved by using gain-controlled edfa and pre-shaped simplex code,” *IEEE Sensors Journal*, vol. 17, no. 11, pp. 3346–3353, 2017.

[69] D. Chai, H. Zhang, Y. Gao, and B. Jin, “Derived sequences decoding approach for long-range distributed temperature sensors,” *IEEE Sensors Journal*, vol. 23, no. 3, pp. 2204–2210, 2023.

[70] S. Babu and R. Kumar, “1d-bernoulli chaos sequences based collaborative-cdma: A novel secure high capacity cdma scheme,” *Wireless Personal Communications*, vol. 96, pp. 2077–2086, 09 2017.

[71] Z. Zhang, H. Wang, Y. Zhao, J. Liu, and L. Yang, “Frequency modulated radar signal with combined chaotic sequence based on bernoulli map,” *Journal of Communications Technology and Electronics*, vol. 61, pp. 971–979, 08 2016.